Cell Reports

Article

# Axonal plasticity in response to active forces generated through magnetic nano-pulling

## Graphical abstract

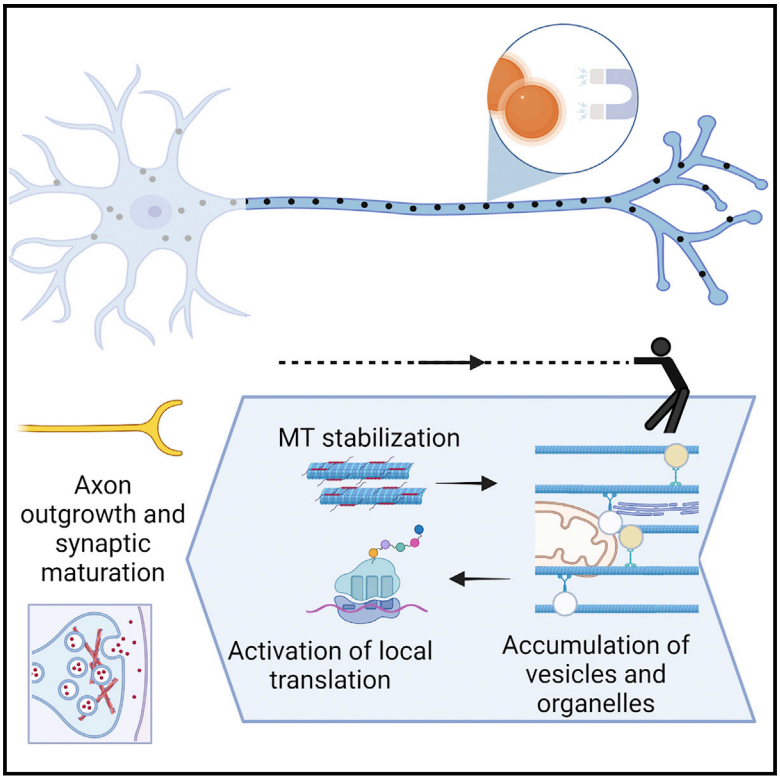


## Authors

Alessandro Falconieri, Sara De Vincentiis, Valentina Cappello, ..., Ugo Borello, Michael Krieg, Vittoria Raffa

## Correspondence

alessandro.falconieri@biologia.unipi.it (A.F.),
vittoria.raffa@unipi.it (V.R.)

## In brief

Falconieri et al. show how mechanical force shapes axonal remodeling through fine modulation of the axonal cytoskeleton. The increase in microtubule assembly results in accumulation of organelles and vesicles, which, in turn, increases the probability of local translational events, leading to mass addition and neuronal maturation.

## Highlights

- Active forces generated through magnetic nano-pulling induce axonal remodeling
- Nano-pulling induces an increase in axonal microtubules
- The resulting accumulation of organelles and vesicles activates local translation
- The cross-talk between axonal transport and translation leads to mass addition

Falconieri et al., 2023, Cell Reports *42*, 111912
January 31, 2023 
https://doi.org/10.1016/j.celrep.2022.111912

CellPress

Cell Reports

CellPress
OPEN ACCESS

Article

# Axonal plasticity in response to active forces generated through magnetic nano-pulling

Alessandro Falconieri,[1,7,*] Sara De Vincentiis,[1,2,7] Valentina Cappello,[3] Domenica Convertino,[4] Ravi Das,[2] Samuele Ghignoli,[1] Sofia Figoli,[1] Stefano Luin,[5] Frederic Català-Castro,[2] Laura Marchetti,[4,6] Ugo Borello,[1] Michael Krieg,[2] and Vittoria Raffa[1,8,*]

[1]Department of Biology, Università di Pisa, 56127 Pisa, Italy
[2]The Barcelona Institute of Science and Technology, Institut de Ciències Fotòniques, ICFO, 08860 Castelldefels, Spain
[3]Center for Materials Interfaces, Istituto Italiano di Tecnologia, 56025 Pontedera, Italy
[4]Center for Nanotechnology Innovation @NEST, Istituto Italiano di Tecnologia, 56127 Pisa, Italy
[5]National Enterprise for NanoScience and NanoTechnology (NEST) Laboratory, Scuola Normale Superiore, 56127 Pisa, Italy
[6]Department of Pharmacy, Università di Pisa, 56126 Pisa, Italy
[7]These authors contributed equally
[8]Lead contact
*Correspondence: alessandro.falconieri@biologia.unipi.it (A.F.), vittoria.raffa@unipi.it (V.R.)
https://doi.org/10.1016/j.celrep.2022.111912

## SUMMARY

Mechanical force is crucial in guiding axon outgrowth before and after synapse formation. This process is referred to as "stretch growth." However, how neurons transduce mechanical input into signaling pathways remains poorly understood. Another open question is how stretch growth is coupled in time with the intercalated addition of new mass along the entire axon. Here, we demonstrate that active mechanical force generated by magnetic nano-pulling induces remodeling of the axonal cytoskeleton. Specifically, the increase in the axonal density of microtubules induced by nano-pulling leads to an accumulation of organelles and signaling vesicles, which, in turn, promotes local translation by increasing the probability of assembly of the "translation factories." Modulation of axonal transport and local translation sustains enhanced axon outgrowth and synapse maturation.

## INTRODUCTION

Mechanical force is one of the major extrinsic factors driving axonal outgrowth.[1,2] Neurons generate the force required for motion during axonal elongation and pathfinding. They transduce exogenous forces into signaling, which makes them mechanosensitive cells. In developing neurons, the growth cone (GC) guides axon extension by detecting guidance cues.[3] The study of the molecular mechanisms governing the trip of the tip highlighted an important contribution from signal mechanotransduction.[4] In GCs, the actin cytoskeleton is connected to the matrix via point contact adhesions. Exogenous pulling forces can trigger maturation of adhesions and acto-myosin contraction, which, in turn, results in advance of the GC through protrusion of actin filopodia/lamellipodia and translocation of microtubules (MTs) in the adhesion site.[5] Some guidance cues, such as nerve growth factor (NGF) and netrin-1, appear to activate the same cascade of events upon binding with their own receptors.[6,7] However, several lines of evidence suggest that the GC is not the only protagonist in signal mechanotransduction in axon outgrowth.[8] First, after connecting with the target, integrated axons continue to grow, accommodating the increase in body mass.[9] Second, neurites can elongate even when GC and filopodial movement is inhibited.[10] Third, stretched axons elongate at a higher rate than the rate imposed by the GC,[11] but they are similar to naturally grown axons in terms of structure and ability to transmit electrical signals.[12] The GC even limits the axon to fully exploit its intrinsic capacity to elongate.[13,14] Recent studies have contradicted the view that mass is added exclusively at the tip, whereas the axon shaft remains stationary. Conversely, intercalated addition of lipids, proteins, vesicles, and organelles along the stretched axon has been demonstrated.[15–17] However, it is not clear which mechanisms underlie addition of these novel components in the axon. Similarly, although the effects of exogenous forces on local remodeling of the GC cytoskeleton are well understood, little is known about the axonal plasticity in response to active mechanical stimuli, mainly because of the limited availability of suitable biophysical tools. Magnetic manipulation is now being used to chronically expose axons of developing neurons to extremely low (picoNewton) mechanical forces.[14,18–26] Briefly, the protocol is based on whole-axon labeling with magnetic nanoparticles (MNPs) as well as use of a magnetic field gradient to generate a magnetic force on MNPs tightly interacting with the elastic components (e.g., cell membranes or the cytoskeletal network) of the axon. The forces generated by magnetic nano-pulling appear to modulate axonal guidance,[23] elongation and sprouting,[22,25] vesicle transport,[18,21,27] neuron polarity,[20] and differentiation of neural

precursor cells.[28] In our study, we used magnetic nano-pulling to answer some open questions regarding the role of external forces on axon outgrowth. Does the stretch induce axonal cytoskeleton remodeling? Is this related to addition of novel components? How is this linked to axon outgrowth and synaptogenesis? We focused on the contribution of axonal MTs, alteration of the local transcriptome, and local mechanisms responsible for mass addition; i.e., local transport, local translation, and the cross-talk between them in response to stimulation.

## RESULTS

### Nano-pulling modifies the axonal transcriptome

To demonstrate that nano-pulling has an effect on the axonal transcriptome, we took advantage of a multi-chamber microfluidic device to spatially segregate mouse hippocampal axons from their cell bodies and dendrites (Figure 1A1).[29,30] When these axons undergo nano-pulling, they increase significantly in length (526.9 ± 22.2 μm and 719.4 ± 17.52 μm for control and stretched axons, respectively; the stretching time [$t_s$] was 120 h, $p < 0.0001$; Figure 1A2), in line with similar data already published by our team.[22,25] To gain an overall perspective of the changes induced by nano-pulling in axonal RNAs, we performed RNA sequencing of axons (Axon-Seq).[31] RNA was isolated from the somato-dendritic and axonal compartments from day *in vitro* 6 (DIV6) hippocampal neurons under control and stretched ($t_s$ = 120 h) conditions (n = 6). Principal-component analysis (PCA) showed that the two compartments have distinct transcriptional profiles (Figure 1B). We found 907 differentially expressed genes (adjusted p value, padj $\leq$ 0.01 and $-2 \leq$ log2 fold change $\leq$ 2) in axons, and gene ontology (GO) was carried out to investigate which cellular processes were misregulated between the two conditions. We used the database for annotation, visualization and integrated discovery (DAVID) to classify the differentially expressed genes based on the cellular components to which they are related.[32] Using these criteria, we found many functional categories which had more than 10 transcripts identified as relevant for axons or related processes: organelles (GO:0005794, Golgi apparatus; GO:0005739, mitochondrion; GO:0005783, endoplasmic reticulum), vesicles (GO:0005764, lysosome; GO:0005765, lysosomal membrane; GO:0005768, endosome; GO:0005770, late endosome [LE]; GO:0031902; LE membrane), membrane (GO:0016020, membrane; GO:0031225, anchored component of membrane), cytoskeleton organization (GO:0005856, cytoskeleton; GO:0005815, microtubule organizing center), and synapse (GO:0045202, synapse). The GO categories identified (Figure 1C; Table S2) reveal many cellular processes that can modulate vesicle trafficking, local transport, local translation machinery, and high energy metabolism, reflecting the need for mass addition and energy demands required to sustain axon outgrowth. The presence of the categories of cytoskeleton and synapse remodeling reflects the potential role of the stimulus in enhancement of neuronal maturation. To deepen our knowledge, we analyzed the 61 dysregulated genes related to the cytoskeleton (GO:0005856). In line with evidence of alterations in MT density and axonal transport, we found that many upregulated genes are related to MT cytoskeleton organization, MT-binding proteins, and MT motor proteins (Figure 1D; Table S3).

The SynGO tool was used to carry out the same analysis at the synaptic level.[33] There were many genes involved in pre- and post-synaptic dynamics that were found to be differentially expressed in stretched axons compared with controls. At the first level of the GO enrichment analysis (GOEA), the first-level categories with 100 or more unique genes were synapse organization (GO:0050808, 306 annotated genes), process in the pre-synapse (269 annotated genes), process in the post-synapse (218 annotated genes), and synaptic signaling (GO:0099536, 193 annotated genes). The second-level categories with 50 or more unique genes were synapse assembly (GO:0007416, 93 annotated genes), post-synapse organization (GO:0099173, 71 annotated genes), synaptic vesicle cycle (GO:0099504, 73 annotated genes), regulation of post-synaptic membrane neurotransmitter receptor levels (GO:0099072, 121 annotated genes), regulation of post-synaptic membrane potential (GO:0060078, 55 annotated genes), and trans-synaptic signaling (GO:0099537, 185 annotated genes) (Figure 1E).

The next sections provide insights into the cellular processes identified by GO analysis of Axon-Seq data (axonal MT cytoskeleton organization, organelles, vesicular transport, mass addition, and synapse organization).

### Axonal MTs sustain stretch growth

We then used transmission electron microscopy (TEM) analysis to understand whether the force generated by nano-pulling induces remodeling of the neurite cytoskeleton. In stretched samples, MTs maintained their morphology and integrity (Figures 2A1 and 2A2). After 120 h of stimulation, we found a 36% increase in MT linear density in stretched neurites (from 6.05 ± 0.37 $\mu m^{-1}$ for the control to 8.23 ± 0.44 $\mu m^{-1}$ for the stretched group, $p = 0.0041$; Figure 2A3). So why do MTs respond to force, and how does force influence MT dynamics? We estimated the ratio of acetylated versus tyrosinated MTs as a hallmark of MT stability in developing axons.[34] In control axons, the ratio of acetylated versus tyrosinated α-tubulin showed a distribution (minimum, 1.02; maximum, 3.90; mean, 2.18) that was very similar to the one reported previously for stage 3 axons of hippocampal neurons ($1 \leq$ ratio $\leq 4$).[34] The mean value of the data distribution was statistically different between stretched and control axons (Figure 2A4; $p = 0.03$), and the minimum value of data distribution did not change, as expected (minimum, 1.00), in contrast to the maximum value (4.71).

Then we tested the hypothesis that direct perturbation of MT organization disrupts stretch growth. We used the *C. elegans* model and found, similarly to mouse hippocampal neurons, a significantly increased length of axons of wild-type touch receptor neurons (Figure 2B1; $p < 0.0001$) or motor neurons (Figure S2A; $p < 0.0001$) under the stretched condition. We then repeated the assay with the *C. elegans* strain mutated in *mec-12*, encoding for the major α-tubulin in touch receptor neurons, which is then assembled into 15 protofilament MTs together with MEC-7.[35,36] We found no difference in axon length between control and stretched samples (Figure 2B1; $p = 0.49$), suggesting that the *C. elegans* neurons lacking α-tubulin do not respond to nano-pulling. To corroborate these findings, we used a mutant strain with a *mec-7* allele in touch receptor neurons that lacks stable *in vivo* protofilament MTs but still forms 11 small-diameter

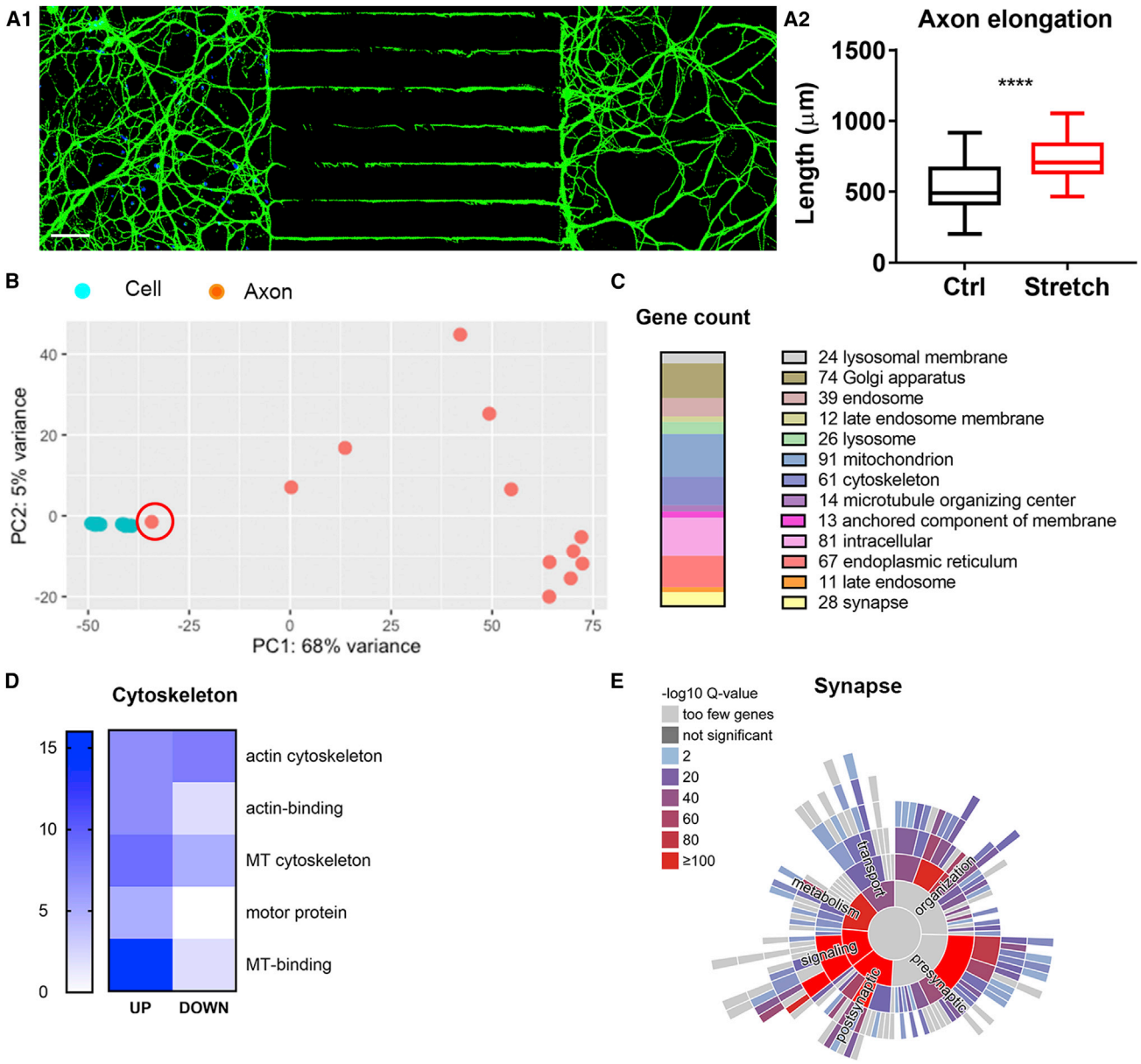


**Figure 1. Axon-Seq of control and stretched axons of hippocampal neurons**

(A1) DIV6 hippocampal neurons cultured in XONA microfluidic chambers (TUBB3, green; DAPI, blue; scale bar, 50 μm).

(A2) Axon lengths in the axon compartment (stretching time [$t_s$] = 120 h). Boxplot (min to max), n = 60 axons from five biological replicates, unpaired *t* test, 2-tailed, $p < 0.0001$, t = 6.807, degrees of freedom (df) = 118.

(B) PCA. The circled sample highlights an axonal sample contaminated with the somatic component that was excluded from further analysis (STAR Methods).

(C) GO via DAVID software, functional annotation chart, and GOterm_cc_direct. The graph plots only the axonal or axon-related categories or categories with fewer than 10 annotated genes. Some general categories (GO:0005737, cytoplasm; GO:0016020, membrane; GO:0005829, cytosol) were not included, but the full list is given in Table S2.

(D) Cytoskeleton GO analysis (GO:0005738), manual annotation. The bar plots the gene number. A gene table is provided in Table S3.

(E) Synaptic GO analysis via SynGO, function domain, and enrichment analysis.

protofilament MTs.[37] We reasoned that MTs are destabilized at higher temperatures (16°C versus 25°C) because of their faster depolymerization rate at 25°C.[38] In line with this rationale, the axon length of stretched samples at 16°C was significantly increased compared with the control (unstretched, $p < 0.0001$), whereas neurons cultured at 25°C showed no differences between stretched and control conditions (Figure 2B2; $p = 0.99$). This strongly suggests that stretch growth is dependent on functional β-tubulin. To validate that stretch growth is not systemically inhibited at 25°C, we cultured wild-type touch receptor neurons

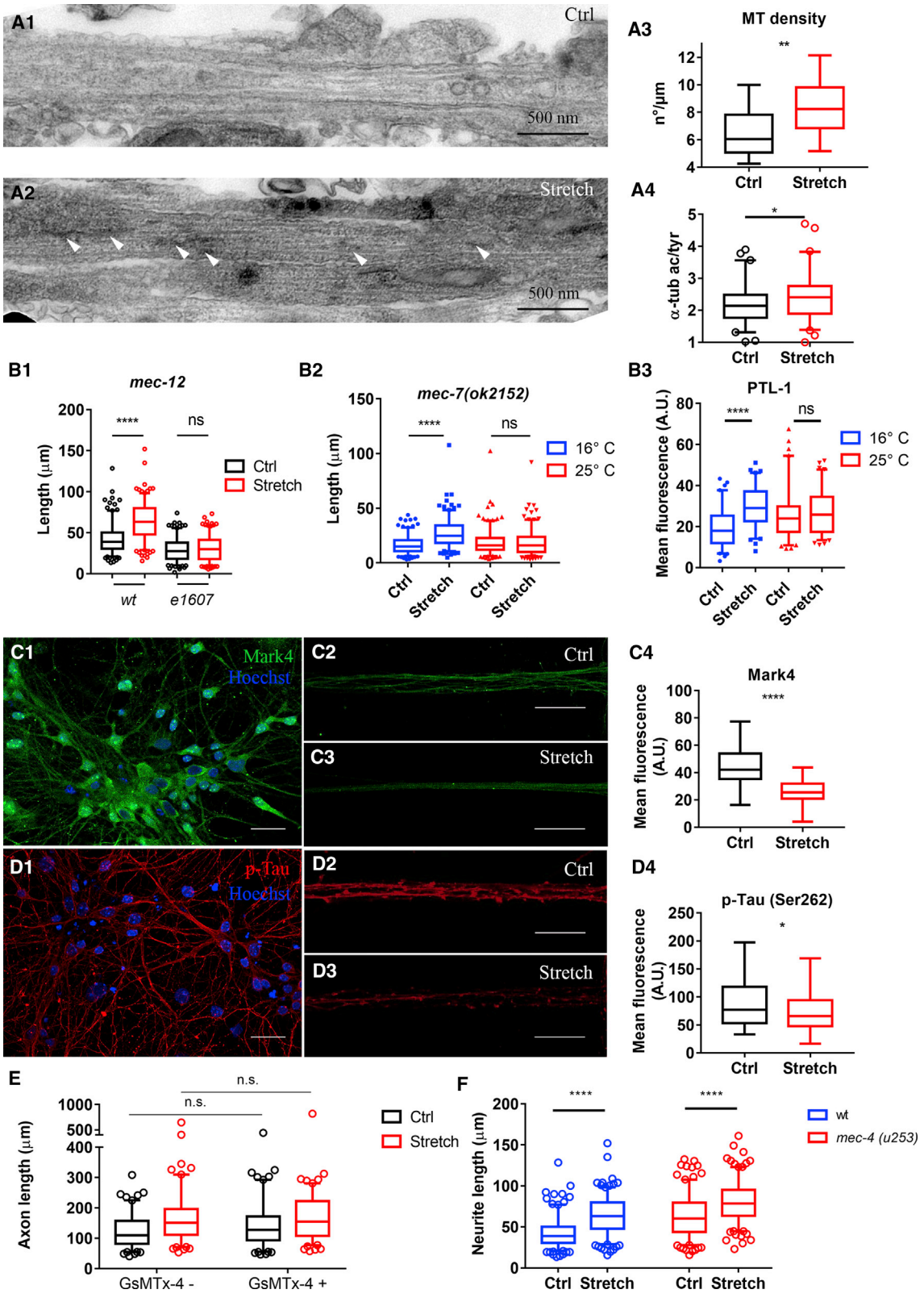


(legend on next page)

at various temperatures. Even though the absolute axon length at lower temperature was shorter, we observed stretch growth at 16°C and 25°C (Figure S2B). These data confirm our previous observation[25] that stretch growth depends on MT formation. We also quantified the fluorescence levels of PTL-1, an MT-associated protein with tau-like repeats,[39] as a marker of MT abundance. We leveraged a transgenic animal strain with an mNeonGreen insertion at the endogenous *ptl-1* locus[40] in the background of the same *mec-7* mutant allele as described above. At 16°C, we found a strong increase in the level of PTL-1 total fluorescence (Figure S2C; $p < 0.0001$) and mean fluorescence (Figure 2B3; $p < 0.0001$) in stimulated axons, whereas at 25°C, there were no differences between control and pulled samples (total fluorescence, $p > 0.999$; Figure S2C; mean fluorescence, $p > 0.999$; Figure 2B3). Considering that no differences in the length of control and stretched axons were observed at 25°C, this indicates that the levels of the MT-associated protein PTL-1 increase during stretch growth. The increase in the length of stretched axons at 16°C can explain the increase in PTL-1 total fluorescence but not the increase in PTL-1 mean fluorescence, which can be explained by an increase in MT density.

We also tested the possible involvement of MT-associated proteins (MAPs) in hippocampal neurons because they are another possible target that modulates the stability/instability dynamics of MTs in *vivo*.[41,42] We focused on TAU for the following reasons: (1) TAU phosphorylation influences MT assembly,[43] (2) re-positioning of TAU has already been found in response to force,[20] and (3) we found down-regulation of MT affinity-regulating kinase 4 (MARK4), which phosphorylates TAU on Ser-262, via Axon-Seq. Phosphorylation of TAU in the Ser-262 residue considerably reduces its binding to MTs, causing MT destabilization.[44–46] Conversely, when TAU is dephosphorylated, it may promote MT assembly.[47–49] Here we estimated the levels of MARK4 and TAU (Ser-262) in stretched versus control axons by immunofluorescence and quantification of the mean fluorescence signal (Figures 2C and 2D). The levels of the kinase (Figure 2C4; $p < 0.0001$) and its target (Figure 2D4; $p = 0.01$) were decreased in stimulated axons. Tension-dependent down-regulation of MARK4 could be another mechanism contributing to MT stabilization by decreasing the levels of TAU (Ser-262).

As a next step, we wanted to determine whether other mechanotransducers are required for force transduction mediated by nano-pulling. Because the plasma membrane is involved in mechanosensing via mechanosensitive ion channels (MSCs), mouse hippocampal neurons were treated with GsMTx-4, a spider venom peptide that inhibits cationic MSCs.[50–53] We treated hippocampal neurons with 500 nM GsMTx-4, a dose that was found to block cationic MSCs in cortical neurons.[52,53] We did not find statistically significant differences in axon length in control neurons (Figure 2E; control [Ctrl]: GsMTx-4$^-$ versus GsMTx-4$^+$, $p > 0.05$), excluding an influence on axon length by the treatment *per se*. There was no statistically significant difference in axon length in stretched neurons (Figure 2E; stretch: GsMTx-4$^-$ versus GsMTx-4$^+$, $p > 0.99$). To verify the hypothesis that MSCs are not major players in nano-pulling-mediated force transduction, we used a *C. elegans* strain mutated in *mec-4*, which encodes for the protein responsible for mechanosensing in touch receptor neurons.[54] Our data showed that touch receptor neurons lacking *mec-4* undergo stretch growth (Figure 2F; *mec-4(u253)*: Ctrl versus stretch, $p < 0.0001$), suggesting that functional MEC-4 is not essential for nano-pulling.

**Figure 2. Axon remodeling in response to nano-pulling**

(A, C, and D) DIV6 hippocampal neurons ($t_s$ = 120 h).

(B) DIV3 *C. elegans* neurons ($t_s$ = 48 h).

(E) DIV3 hippocampal neurons ($t_s$ = 48 h).

(B and F) DIV3 *C. elegans* neurons ($t_s$ = 48 h).

(A1 and A2) TEM images of cross-sections of Ctrl neurites (A1) and stretched ones (A2). Arrowheads indicate the ER.

(A3) Quantification of MT linear density; n = 21 neurites from two biological replicates. Boxplot (min to max), unpaired *t* test, 2-tailed, p = 0.0041, t = 3.042 df = 40.

(A4) Ratio of acetylated versus tyrosinated α-tubulin. Boxplot (5th–95th percentiles), n = 60 axons from six biological replicates, unpaired *t* test, 2-tailed, p = 0.03, t = 2.131, df = 118.

(B1) Axonal length of wild-type (WT) and α-tubulin KO touch receptor neurons (*mec-12(e1607)*) in the Ctrl and stretched conditions. Boxplot (5–95 percentile), n = 200 neurons from four biological replicates. Kruskal-Wallis test with post hoc Dunn's test, $p < 0.0001$.

(B2) Axonal length of touch receptor neurons in a β-tubulin loss-of-function background (*mec-7(ok2152)*), lacking stable 15 protofilament MTs. Ctrl and stretched axons were measured at 16°C and at 25°C. Boxplot (5–95 percentile), n = 200 axons from four biological replicates, Kruskal-Wallis test with post hoc Dunn's test, $p < 0.0001$.

(B3) Quantification of mNeonGreen (mNG) mean fluorescence in a transgenic model of tagged mNG::PTL-1 in the background of the same mutant (*mec-7(ok2152)* at 16°C and at 25°C. Boxplot (5th–95th percentiles), n = 80 axons from four biological replicates, Kruskal-Wallis test with post hoc Dunn's test, $p < 0.0001$.

(C1–C3) Immunohistochemistry against MARK4 (C1, green) in Ctrl axons (C2) and stretched ones (C3). Scale bars, 25 μm (C1) and 20 μm (C2 and C3).

(C4) Quantification of MARK4 mean fluorescence. Boxplot (min to max), n = 80 microfluidic channels from four biological replicates; unpaired *t* test, 2-tailed, $p < 0.0001$, t = 10.27, df = 163.

(D1–D3) The specific target of MARK4 kinase, TAU (Ser-262) (D1, red), was evaluated in Ctrl (D2) and stretched (D3) axons. Scale bars, 25 μm (D1) and 20 μm (D2 and D3).

(D4) Quantification of TAU (Ser-262) mean fluorescence. Boxplot (min to max), n = 80 microfluidic channels from four biological replicates, Mann-Whitney test, $p < 0.0001$.

(E) Axon length in response to GsMTx-4 (500 nM). Boxplot (5th–95th percentiles), n = 120 axons from four biological replicates, two-way ANOVA with post hoc Sidak's test. Row factor (with or without GsMTx-4): p = 0.1, f = 2.732. Column factor (Ctrl versus stretch): $p < 0.0001$, f = 25.92.

(F) Neurite length of touch receptor neurons of *C. elegans* strains encoding for a WT or mutant *mec-4 (mec4(u253))*. Boxplot (5th–95th percentiles), n = 200 axons from four biological replicates, two-way ANOVA with post hoc Sidak's test. Row factor (Ctrl versus stretch): $p < 0.0001$, f = 153.7. Column factor (strain): $p < 0.0001$, f = 140.2.

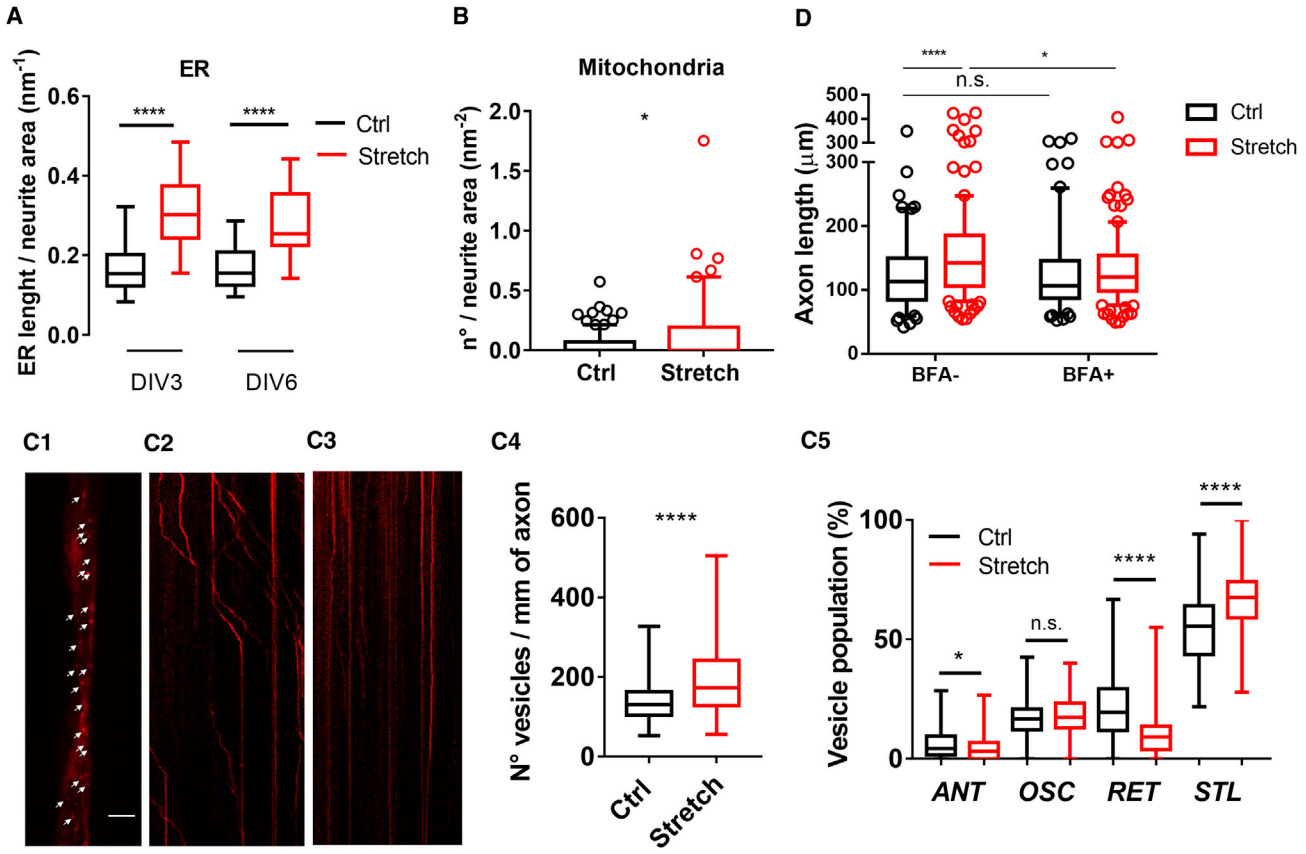


**Figure 3. Axonal transport of vesicles and organelles**

(A) Density of ER (nm of tubules/nm$^2$ of neurite area) in Ctrl and stretched ($t_s$ = 2 and 5 days) neurites of DIV3 and DIV6 hippocampal neurons. Boxplot (min to max), n = 20 neurites from two biological replicates, one-way ANOVA with post hoc Tukey's comparison, p < 0.0001, f = 22.22.

(B) Density of mitochondria (number/nm$^2$ of axon area) in Ctrl and stretched ($t_s$ = 13 days) neurites of DIV14 hippocampal neurons. Boxplot (5th–95th percentiles), n = 20 axons from two biological replicates, unpaired *t* test, 2-tailed, p = 0.0087, t = 2,773 df = 38.

(C) Tracking analysis of axonal NGF vesicles in DRG neurons cultured in the microfluidic devices.

(C1) NGF vesicles (white arrows) in the microfluidic channels.

(C2 and C3) Representative kymographs of the time-dependent displacement of Alexa 647-labeled NGF vesicles along a single axon in the Ctrl group (C2) and the stretched group (C3); x-scale bar, 10 µm; y-scale bar, 5 s.

(C4) Total mean population percentages: increase in stalled vesicles and decrease in RET ones in stretched groups compared with Ctrl. Boxplot (min to max), three biological replicates, Mann-Whitney test: ANT (p = 0.01), OSC (p = 0.12), RET (p < 0.0001), STL (p < 0.0001).

(C5) Density of NGF vesicles under the two conditions: increase in the total number of NGF vesicles in the stretched group compared with spontaneous elongation. Boxplot (min to max), three biological replicates, Mann-Whitney test, p < 0.0001. NGF (red) in (C1)–(C3). Scale bars, 5 µm.

(D) Axon length in response to BFA (50 ng mL$^{-1}$). DIV3 hippocampal neurons ($t_s$ = 48 h). Boxplot (5th–95th percentiles), n = 120 axons from four biological replicates, two-way ANOVA with post hoc Sidak's test. Row factor (with or without BFA): p = 0.029, f = 4.807. Column factor (Ctrl versus stretch): p < 0.0001, f = 16.74.

## Nano-pulling modulates axonal transport

In the axon, transport of many organelles and vesicles is linked to MTs and MT stability. We analyzed the distribution of endoplasmic reticulum (ERs), which appear as ribosome-free membranous structures with a tubular shape parallel to the plasma membrane of neurites (Figure 2A2, white arrowheads). We found a strong accumulation of ERs in response to nano-pulling (Figure 3A). The ER density was 0.17 ± 0.014 and 0.31 ± 0.018 nm per nm$^2$ of neurite area for the Ctrl and stretched groups at DIV3 ($t_s$ = 24 h, p < 0.0001), and this trend continued over the following days (0.17 ± 0.012 nm$^{-1}$ for the Ctrl and 0.28 ± 0.082 nm$^{-1}$ for the stretched group at DIV6, corresponding to $t_s$ = 120 h, p < 0.0001). At later time points (DIV14, corresponding to $t_s$ = 13 days), we found a strong increase in the density of mitochondria in neurites (0.052 ± 0.011 and 0.127 ± 0.024 mitochondria/nm$^2$ of neurite area for the Ctrl and stretched groups, respectively; p = 0.04) in response to the high energy demand of stretched neurites (Figure 3B). We found mitochondria in 25% and 34.3% of cross-sections for the Ctrl and stretched neurites, respectively; when limiting the analysis to cross-sections that were positive for the presence of mitochondria, we still found a similar trend (0.207 ± 0.022 and 0.371 ± 0.051 mitocondria/nm$^2$ for the Ctrl and stretched neurites, respectively; p = 0.002).

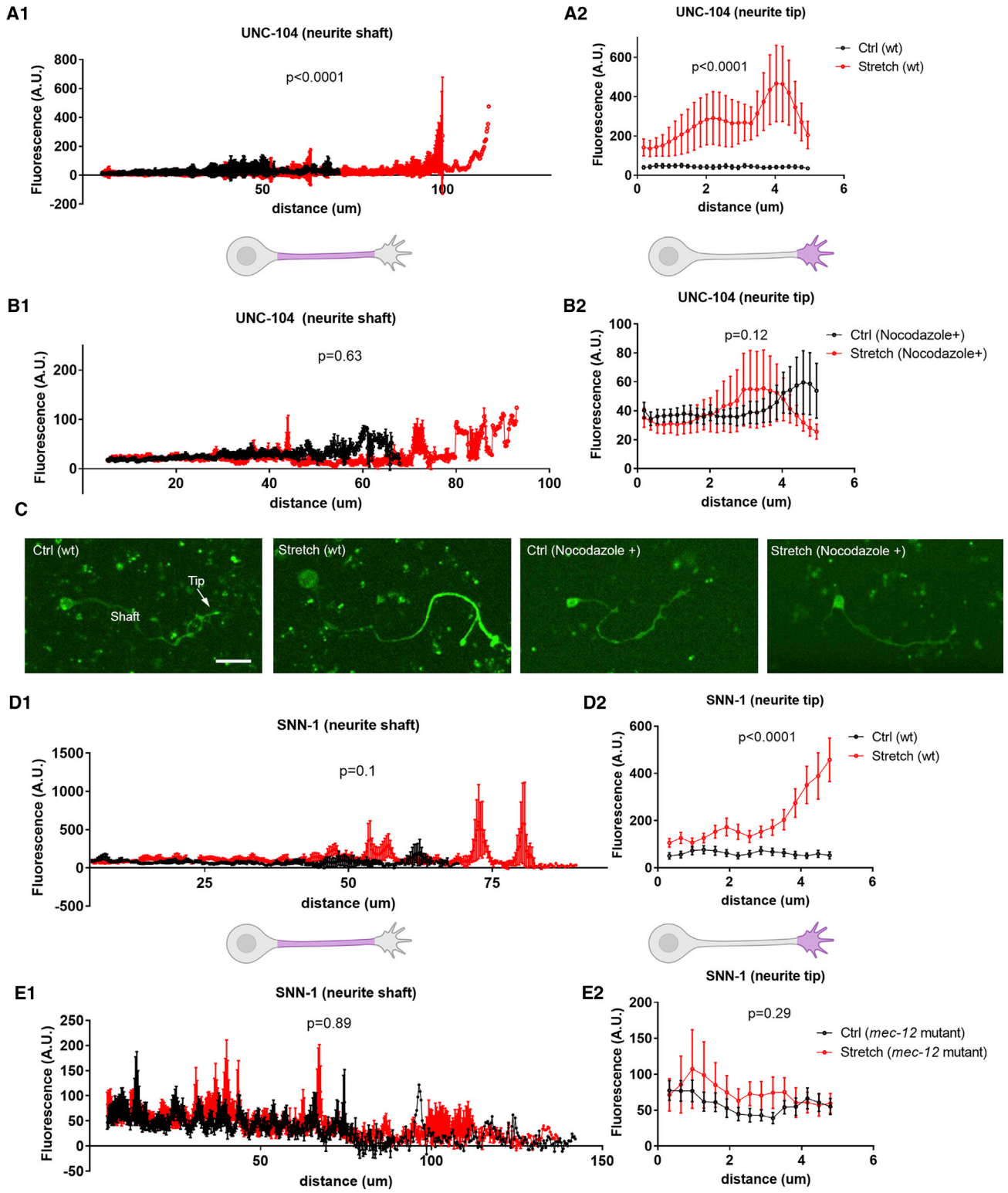


**Figure 4. Monitoring UNC-104 motor protein and synapsin SNN-1 in *C. elegans***

(A and B) Stretch growth assay in a *C. elegans* strain encoding for fluorescent UNC-104 without (A1 and A2) or with (B1 and B2) nocodazole treatment (1.8 ng $mL^{-1}$). Shown is the UNC-104 fluorescence signal (mean ± SEM) in the shaft (A1 and B1) and tip (A2 and B2) of neurites of DIV3 touch receptor neurons ($t_s$ = 48 h). Linear regression analysis, n = 20 neurites from four biological replicates. Without nocodazole treatment: neurite shaft (p < 0.0001, F = 22.91, df numerator (DFn) =

*(legend continued on next page)*

Next we investigated whether alteration of transport also affects other components, such as signaling vesicles transporting the trophic factors sustaining axon growth.[55] NGF was fluorescently labeled and added to the cell growth medium, and axonal trafficking of NGF signaling vesicles was tracked in dorsal root ganglion (DRG) neurons (Figure 3C1) in the presence and absence of the stimulus (Figures 3C2 and 3C3). To evaluate the effect of forces on the rate of fast axonal transport, we characterized the retrograde (RET), anterograde (ANT), oscillating (OSC), and stalling (STL) components by single-vesicle imaging and tracking (Video S1), as reported previously.[56] Under stimulation, there is a clear accumulation of vesicles in the axon shaft (Video S2). 30 min after magnet removal, axons seem to rescue the levels of Ctrl cultures (Video S3). Quantitative data analysis confirmed an overall increase in NGF vesicles in the shaft of stretched axons compared with spontaneous elongation (Figure 3C4; $p < 0.0001$). However, vesicle accumulation is not the consequence of the increase in the ANT component. Mechanical stimulation led to a strong reduction of RET components ($p = 0.01$) and a corresponding increase in STL ones ($p < 0.0001$) (Figure 3C5). This result was also confirmed by kymograph analysis, which showed more vertical lines in the kymograph of the stretched group, indicating an increased number of stationary vesicles (Figure 3C3). On the other hand, the kymograph of the Ctrl group showed diagonal lines representing moving vesicles (Figure 3C2). This suggests a tendency toward RET vesicles so that they stall in response to the tension.

Next we decided to investigate how stretch growth is influenced by alteration of vesicular trafficking. We performed pharmacological treatment using brefeldin A (BFA), a global inhibitor of vesicle trafficking by targeting Golgi apparatus-mediated vesicle secretion.[57,58] The treatment resulted in a reduction in the length of stretched axons (Figure 3D; stretch, $BFA^-$ versus $BFA^+$, $p < 0.05$) but the treatment *per se* did not influence axon length (Figure 3D; Ctrl, $BFA^-$ versus $BFA^+$, $p = 0.99$). One possible interpretation of this result is that the MT stabilization induced by nano-pulling could alter axonal transport, which, in turn, is required to modulate axon outgrowth. To validate this hypothesis, we used the *C. elegans* model to fluorescently label UNC-104, a motor protein involved in MT-associated ANT transport and orthologous to several human genes, including KIF1A and KIF1B.[59] A statistically significant enrichment in motor protein fluorescence distribution was found in stretched neurites at the level of the neurite shaft (Figure 4A1; $p < 0.0001$) and the neurite tip (Figure 4A2; $p < 0.0001$) To test the hypothesis that this difference can be directly linked to the increase of MT density observed in stretched axons, we repeated the experiments in the presence of nocodazole (an MT de-stabilizing agent)[60] by using a concentration tested previously in primary neurons.[25] As expected, the treatment did not affect the UNC-104 fluorescence distribution under Ctrl conditions (Ctrl, neurite tip: $nocodazole^-$ versus $nocodazole^+$, $p = 0.70$; Ctrl, neurite shaft: $nocodazole^-$ versus $nocodazole^+$, $p = 0.16$). However, the same dose blocked stretch growth because no difference could be detected in neurite length (Figure S3; $p = 0.08$) or UNC-104 signal between Ctrl and stretched axons at the level of the shaft (Figure 4B1; $nocodazole^+$: Ctrl versus stretch, $p = 0.63$) or the tip (Figure 4B2; $nocodazole^+$: Ctrl versus stretch, $p = 0.12$). In *C. elegans*, UNC-104 is used for ANT translocation of synaptic vesicles.[59] Thus, we decided to use a *C. elegans* strain encoding for a fluorescent synapsin, SNN-1. No statistically significant differences between the SNN-1 fluorescence distribution in the Ctrl and stretched neurites were observed at the level of the shaft (Figure 4D1; $p = 0.1$), whereas a strong difference was present at the tip level (Figure 4D2; $p < 0.0001$). The enrichment at the tip (but not in the shaft) is likely to be related to accumulation of synapsin vesicles through association with the actin cytoskeleton of the pre-synaptic terminals.[61] By analyzing the same data in a *C. elegans mec-12* mutant, no statistically significant differences in SNN-1 fluorescence were found in the distribution at the neurite shaft (Figure 4E1; $p = 0.89$) or at the tip (Figure 4E2; $p = 0.29$). The collected data suggest that, in stretched axons, MT stability is required for accumulation of UNC-104, UNC-104-related vesicles, and neurite outgrowth.

## Nano-pulling activates local translation

Axonal transport and local translation are the two main mechanisms that sustain addition of mass in the axon. In a previous study, we found that the cycloheximide (CH), a potent inhibitor of protein synthesis,[62] blocked stretch growth of hippocampal neurons ($t_s$ = 48 h).[25] Consistent with previous studies, we observed a similar impairment after 5 days of stretching (Figure 5A1; $CH^+$, Ctrl versus stretch, $p = 0.99$). The density of MTs in stretched neurites was not affected by the treatment (Figure 5A2; $CH^+$, Ctrl versus stretch, $p = 0.44$), suggesting that activation of translation could be downstream of MT stabilization. We focused the analysis on the axonal level. Local translation has an important role in axon elongation and synapse formation.[63] As a proxy of the rate of axonal translation, we estimated the concentration of axonal ribosomes that are in a stage of active translation by immunofluorescence (Figure 5B1) and quantification of the mean fluorescence signal, respectively, in stretched versus unstretched axons. Experimental data revealed a strong increase in the signals of axons undergoing nano-pulling (mean fluorescence, $p < 0.0001$; Figure 5B2). Ribosomes can be assembled in the nucleolus and transported to the axon or

1, df denominator (DFd) = 943); neurite tip ($p < 0.0001$, $F = 34.91$, DFn = 1, DFd = 50). With nocodazole treatment: neurite shaft ($p = 0.63$, $F = 0.2266$, DFn = 1, DFd = 817); neurite tip ($p = 0.12$, $F = 2.457$, DFn = 1, DFd = 50).

(C) Representative images for each condition.

(D and E) Stretch growth assay in a *C. elegans* strain encoding for fluorescent SNN-1 in WT (D) and *mec-12* mutant (E) strains. Shown is the SNN-1 fluorescence signal (mean ± SEM) in the shaft (D1 and E1) and tip (D2 and E2) of the neurites of DIV3 touch receptor neurons ($t_s$ = 48 h). Linear regression analysis, n = 20 neurites from four biological replicates. WT strain: neurite shaft ($p = 0.1$, $F = 2.714$, DFn = 1, DFd = 460); neurite tip ($p < 0.0001$, $F = 40.19$, DFn = 1, DFd = 21). Mec-12 mutant strain: neurite shaft ($p = 0.89$, $F = 0.01817$, DFn = 1, DFd = 839); neurite tip ($p = 0.29$, $F = 1.178$, DFn = 1, DFd = 26).

The x axis of the plots shows the distance from the end of the cell body (A1, B1, D1, and E1) or the central domain of the GC (A2, B2, D2, and E2). Refer to Figure S3 for a representation of neurite length distribution.

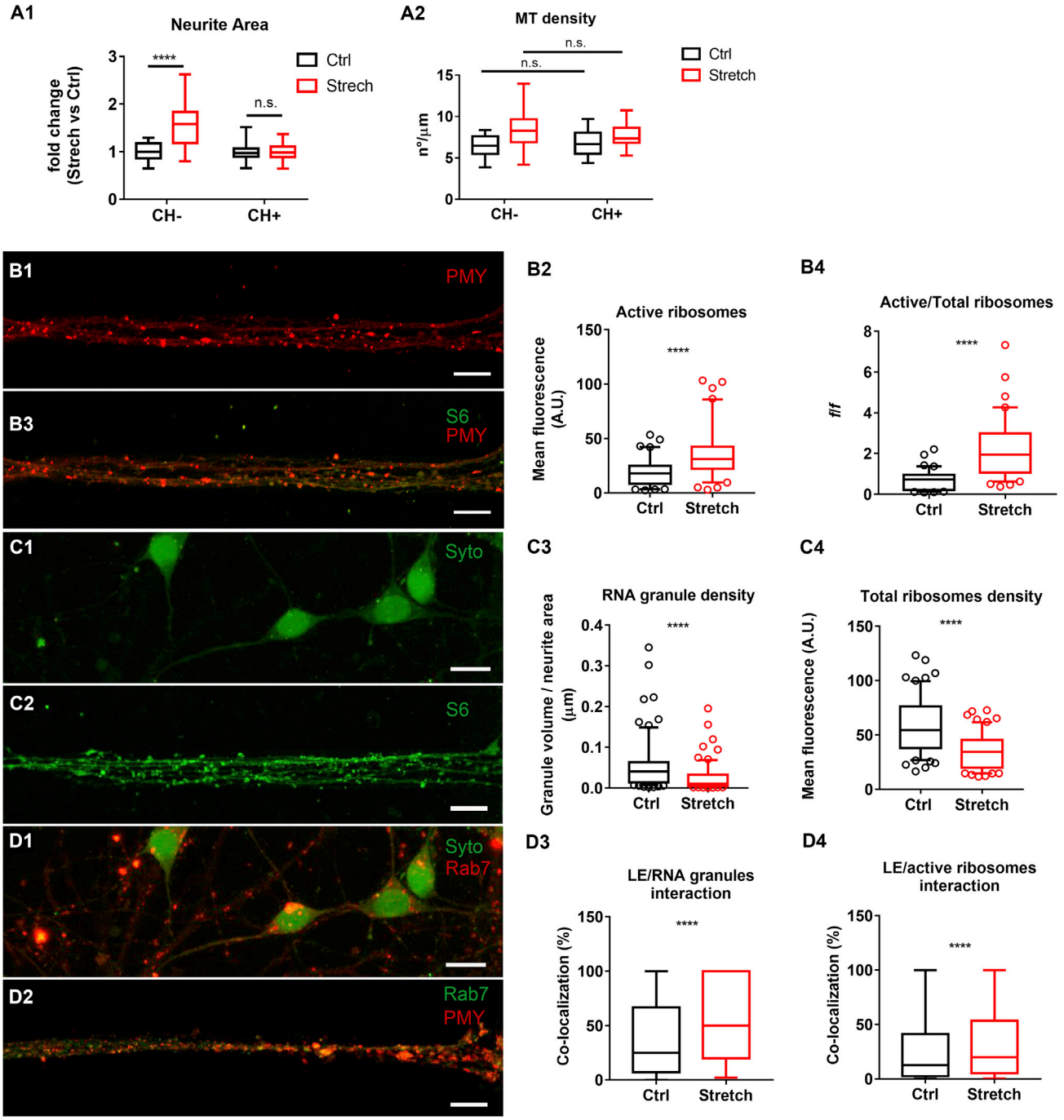


**Figure 5. Activation of local translation after nano-pulling in axons of mouse hippocampal neurons (DIV6, $t_s$ = 120 h)**

(A) Stretch growth in response to CH (30 ng $mL^{-1}$).

(A1) Neurite area. Boxplot (min to max), n = 20 images analyzed from four biological replicates, two-way ANOVA with post hoc Sidak's test. Row factor (with or without CH): $p < 0.0001$, $f = 23.96$. Column factor (Ctrl versus stretch): $p < 0.0001$, $f = 23{,}74$.

(A2) MT linear density. Boxplot (min to max), n = 20 axons from two biological replicates, two-way ANOVA with post hoc Sidak's test.

(B) Row factor (with or without CH): $p = 0.56$, $f = 0.3411$. Column factor (Ctrl versus stretch): $p < 0.0001$, $f = 16.53$.

(B1) Staining of a ribosome in active translation: Puromycin (PMY, red); scale bars, 10 µm.

(B2) Increase in mean fluorescence of active ribosomes in stretched versus Ctrl axons. Boxplot (5th–95th percentiles), n = 80 microfluidic channels from four biological replicates, Mann-Whitney test, $p < 0.0001$.

(B3) Staining of total ribosomes and ribosomes in active translation: PMY (red), S6 (green); scale bars, 10 µm.

*(legend continued on next page)*

assembled locally in the axon in a nucleolus-independent manner.[64–66] Whatever the assembly mechanism, axons appear to have mechanisms to switch on local translation, based on recruitment of vesicles containing RNA granules, such as LEs,[67] lysosomes,[68] and mitochondria.[69] Our evidence suggests that the ratio of active to total ribosomes increases in stretched axons (Figure 5B4; $p < 0.0001$) but that there is no increase in the number of total axonal ribosomes. In fact, we found a lower concentration of ribosomes in stretched axons, suggesting that the pre-assembled ribosomes and the *in situ* ribosomal components dilute and spread in the longer stretched axons (40% decrease in mean fluorescence signal, from 57.59 ± 3.28 for the Ctrl group to 34.74 ± 2.10 for the Stretch group, $p < 0.0001$; Figure 5C4). This idea is supported by the finding that the concentration of RNA granules shows a similar trend (54% decrease in the volume occupied by RNA granules in the axon, normalized to axon area; i.e., 0.057 ± 0.0076 μm and 0.026 ± 0.0042 μm for Ctrl and stretched axons, respectively; $p < 0.0001$; Figure 5C3).

These data suggest that the stimulus triggers local translation by switching the resident ribosomes from an inactive to an active state rather than promoting their assembly or transport. To support this hypothesis, we analyzed the population of LEs. Cioni et al.[67] demonstrated that the translation of proteins in axons takes place through intimate contact between LEs and RNA granules, with LEs becoming the platform for the newly synthesized proteins. To establish whether nano-pulling could have an effect on the interaction of these components, we evaluated the co-localizations between LEs and RNA granules and active ribosomes (Figure 5D2). Experimental data showed a strong increase in the number of functional interactions between LEs and RNA granules (Figure 5D3; $p < 0.0001$) and between LEs and active ribosomes (Figure 5D4; $p < 0.0001$).

## Nano-pulling stimulates synapse remodeling

We studied the localization of synapsin I, a protein associated with synaptic vesicles (SVs) in the synapses of the central nervous system (CNS),[70] as a marker of the initial steps of synapse formation in the developing axon. Because formation of mature synapses comprises several stages, analysis of synapsin I was carried out on hippocampal neurons that were stimulated for 6, 13, and 20 days of stretching (Figure 6A), corresponding to a temporal window spanning from 1 week *in vitro* (DIV6, no synapses) to 3 weeks *in vitro* (DIV21, presence of mature synapses), with 2 weeks as the intermediate stage (DIV14, immature synapses), as reported for normally grown axons.[71] We analyzed the synapsin I vesicles that appeared as fluorescent spots, estimating parameters such as spot volume (Figure 6B), spot density (Figure 6C), and spot fluorescence (Figure 6D) in Ctrl and stretched neurites. These give a rough estimation of vesicle size, vesicle concentration in neurites, and synapsin I concentration in the vesicle, respectively. For Ctrl cultures, we observed, in the experimental time frame, that spots remained constant in volume (Figure 6B; $p = 0.97$) but that the emitted fluorescence (Figure 6D; $p = 0.03$) as well as the density (Figure 6C, $p = 0.02$) of the spots increased at DIV21, corresponding to the time of formation of mature synapses. A multiple comparison among all time points highlights that stimulated neurites always have more spots, irrespective of the time ($p = 0.007$). The spots of stimulated neurites are smaller than Ctrl ones at DIV6 ($p = 0.0003$), but the significance of this difference is totally lost at DIV21 ($p = 0.56$). Our data show that, at DIV21, synapsin $I^+$ spots in stimulated neurites are similar in volume and protein rich but more numerous than Ctrl ones.

To understand whether stimulation could speed up synapse formation, developing axons were analyzed at DIV7 and DIV14 for the presence of SVs, active zone (AZ), synaptic cleft (SC), and pre- and post-synaptic membranes as markers of the presence of a synapse.[72] At DIV7, no hallmarks of synapses were observed under Ctrl conditions (data not shown). Conversely, DIV7 neurons stimulated for 6 days were found to have some developing synapses, characterized by the typical pre- and post-synaptic elements on the two sides of the SC. On the presynaptic side, we observed accumulation of SV pools at different distances from the AZ, whereas, on the post-synaptic side, we noted formation of post-synaptic density (PSD; the specialized region for neurotransmitter recording) (Figures 7A1 and 7A2). The structure of these synapses was very similar to the ones observed in the Ctrl cultures at DIV14 (Figures 7A1 and 7A2 versus Figure 7A3). At DIV14, some synapses of stretched neurons (roughly 15%) were structurally similar to the Ctrl ones in terms of SV density and the presence of MTs (Figure 7A3 versus Figure 7A5). However, approximately 85% appeared to be in a more advanced stage, showing a terminal localization and the curved shape typical of mature synapses. In these mature synapses, we also found some in which the presynaptic terminals appeared to be morphologically different from all others because of a more contrasted cytoplasm (Figure 7A6 versus Figure 7A5). This is probably due to a higher density of SVs and of the actin

(B4) Active ribosomes compared with the total (ratio between fluorescence signals). Boxplot (5th–95th percentiles), n = 80 microfluidic channels from three biological replicates, Mann-Whitney test, $p < 0.0001$.
(C1) Staining of RNA granules: Syto RNA Select (green); scale bars, 10 μm.
(C2) Staining of total ribosomes: S6 (green); scale bars, 10 μm.
(C3) Axonal density of RNA granules expressed as total volume of RNA granules per axon area in Ctrl versus stretched axons. Boxplot (5th–95th percentiles), n = 75 neurites from three biological replicates, Mann-Whitney test, $p < 0.0001$.
(C4) Quantification of mean fluorescence in Ctrl versus stretched axons. Boxplot (5th–95th percentiles), n = 60 microfluidic channels from three biological replicates, Mann-Whitney test, $p < 0.0001$.
(D1) Immunostaining of LEs (Rab7, red) and RNA granules (Syto RNA select, green); scale bars, 10 μm. (D2) Immunostaining of LEs (Rab7, green) and active ribosomes (PMY, red) in axons; scale bars, 10 μm. (D3) Co-localization between LEs and RNA granules in Ctrl versus stretched axons. Boxplot (min to max), n = 75 neurites from three biological replicates, Mann-Whitney test, $p < 0.0001$.
(D4) Co-localization between LEs and active ribosomes in Ctrl versus stretched axons. Boxplot (min to max), n = 53 microfluidics channels from three biological replicates, Mann-Whitney test, $p < 0.0001$.

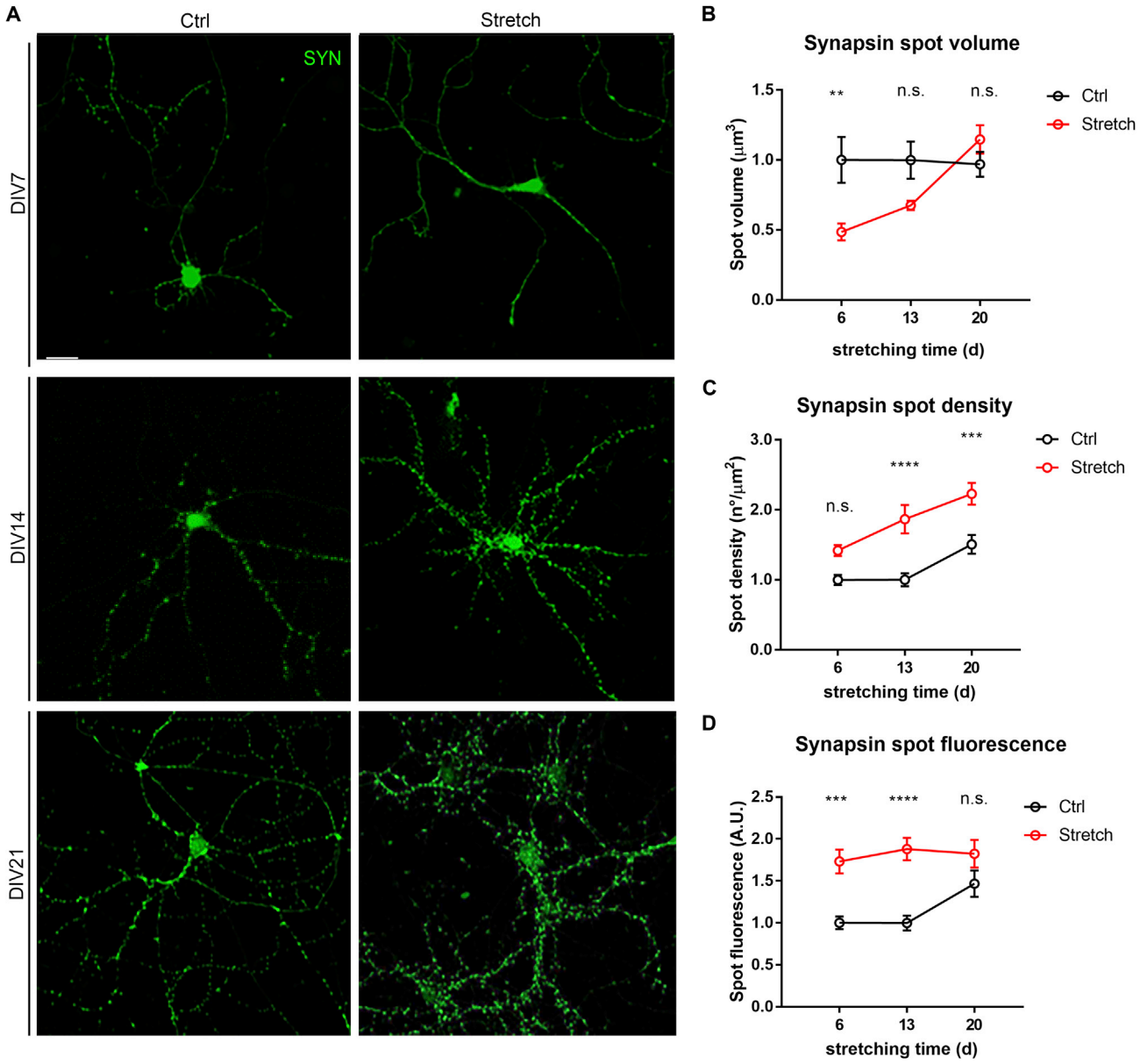


**Figure 6. Axonal localization of synapsin I**

(A) Synapsin I staining (green) of Ctrl and stretched neurons at different $t_s$. Scale bar, 20 µm.

(B–D) Analysis of synapsin I spot volume, (C) spot density, and (D) spot fluorescence after 6, 13, and 20 days of stimulation (corresponding to DIV7, DIV14, and DIV21, respectively) in Ctrl and stretched neurites. Mean ± SEM, n = 30 neurons from three biological replicates, two-way ANOVA with post hoc Sidak's test.

(B) Row factor (Ctrl versus stretch): $p = 0.01$, $f = 4.63$. Column factor (days of stretching): $p = 0.01$, $f = 6.47$.

(C) Row factor (Ctrl versus stretch): $p = 0.007$, $f = 5.03$. Column factor (days of stretching): $p < 0.0001$, $f = 40.47$.

(D) Row factor (Ctrl versus stretch): $p = 0.25$, $f = 1.38$. Column factor (days of stretching): $p < 0.0001$, $f = 38.17$.

filaments to which they are anchored because these are hallmark features of synapse stabilization and maturation.[73] In line with this, we also found an increase in the length of the PSD (147.9 ± 12.84 nm and 287 ± 19.78 nm for the Ctrl and stretch groups, respectively; $p < 0.0001$; Figure 7A4). We also noted an increased number of synapses that show a well-formed PSD (72% in the Ctrl group, 95% in the stretched one). We found no spine specialization at these stages.

To obtain more evidence, the presence of pre- and post-synaptic proteins in close proximity was used as an acceptable criterion for identification of a functional synapse.[74] We measured the co-localization between the presynaptic marker VGlut and the post-synaptic marker Homer1 in neurites at DIV14 (Figure 7B1). There was a significantly higher number of co-localization spots in the stimulated samples than in the Ctrl ones (Figure 7B2; $p < 0.0001$). The coupling probability based on analysis

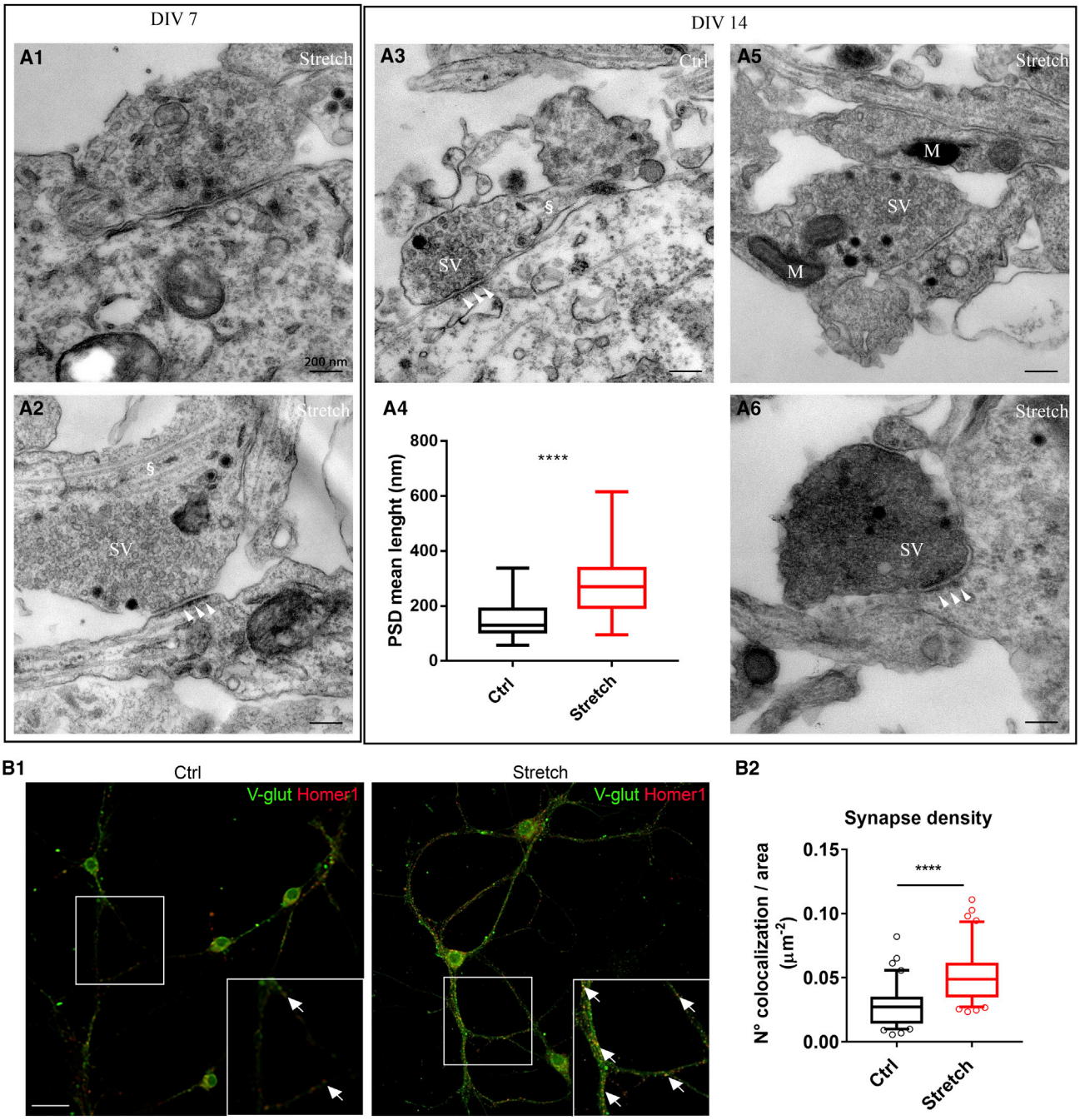


**Figure 7. Synapse remodeling**

(A1–A3, A5, and A6) Micrographs of synapse "draft" at DIV7 (A1 and A2) and DIV14 (A3, A5, and A6), in Ctrl (A3) and stretched (A1, A2, A5, and A6: $t_s$ = 13 days) axons of hippocampal neurons. White arrowheads highlight examples of PSD regions, white § MTs, "M" mitochondrion.

(A4) Length of the PSD region in Ctrl and stretched ($t_s$ = 13 days) axons of DIV14 hippocampal neurons. Boxplot (min to max), n > 28 axons from two biological replicates, Mann-Whitney test, $p < 0.0001$.

(B1) Immunostaining of VGlut1 (green) and Homer1 (red) in hippocampal neurons at DIV14 under Ctrl and stretched conditions ($t_s$ = 13 days). White arrows indicate the co-localizating spots. Scale bar, 20 µm.

(B2) Quantification of synapse density as the number of co-localizing spots in the selected neurite area in the Ctrl and stretched groups. Boxplot (10th–90th percentiles), n = 40 neurons from four biological replicates, Mann-Whitney test, $p < 0.0001$.

of the number of co-localizing spots normalized for the neurite area considered was determined for the two conditions. The number of co-localizations between pre- and post-synaptic markers was 76% ± 12% higher in the stimulated neurites than in the Ctrl groups.

## DISCUSSION

It is well accepted that neurons are under mechanical tension *in vivo* and that they shape neuronal morphology and connectivity.[75,76] During development and axon outgrowth, the GC pulls the axon shaft, and this traction force is responsible for intercalated mass addition.[77] The axon continues to be under traction when the synapse between the axon and its target is established. The growth of the organism increases the distance between the soma and synapse. The mechanical force is an extrinsic signal that induces axon outgrowth, but the molecular pathways of mechanotransduction are still poorly understood in neurons. The tension generated onto axons by magnetic nano-pulling generates an extremely low force and constant loading,[14,18–20,23–26,28] similarly to those exerted, during some phases of development, by tissue morphogenesis or, after development, by the post-synaptic muscle tissue. Here we used a microfluidic chamber model to isolate the axonal compartment from the somato-dendritic one to study axonal remodeling in response to this stimulation. We identified axonal MTs as promising candidates for orchestrating axon outgrowth and intercalated mass addition. We found an increase in the linear density of MTs in stretched neurites. This difference is maintained during stretching (neurite stretching for 48 or 120 h showed a similar increase in MT density compared with the Ctrl, about 36%; Figure 2A3).[25]. This is not an artifact resulting from the "inside" action of MNP-mediated nano-pulling because neurites stretched from the "outside" show a similar ultra-structure in terms of axonal MT accumulation.[78] The crucial role of MTs as a component of signal mechanotransduction was also corroborated by analysis of the axonal transcriptome, which revealed the many genes related to MT structure, MT-binding proteins, and MT axonal transport that were differentially expressed between the stretched and the unstretched conditions (Figure 1D; Table S3). It is still not clear how the mechanical force can induce accumulation of MTs in neurites. MSCs are probably not essential for this signal mechanotransduction. Evidence is lacking that mec-4 is functional in vitro and that touch receptor neurons sense mechanical stretch using MSCs. Along those lines, touch receptor neurons isolated from a *C. elegans* strain mutated in *mec-4*, the gene that regulates mechanosensing in these neurons *in vivo*, still maintain their ability to respond to stretch growth *in vitro* (Figure 2F). It is possible that the MTs are mechanosensitive themselves because direct application of force induces their stabilization,[79] and our data support this hypothesis (Figure 2A4). In *in vitro* assays, MT bundles are able to self-organize and align in the direction of stretch.[80] The effect of tension on MTs is direct, and an increase in traction force can slow down MT depolymerization or disassembly.[79,81] In mammalian cells, the increase in tensile force generated at the adhesion point was found to promote MT assembly.[82] Alternatively, indirect stabilization of MTs can be mediated by MAPs that modulate the stability/instability dynamics of MTs,[41] especially in light of some evidence demonstrating that physical forces can regulate the activity of MAPs. A tensile force applied to proteins that bind to the plus ends of MTs, such as XMAP215 in *Xenopus*[42] and Dam1 in yeast,[83] was found to increase MT length. In this regard, we formulated the data-driven (RNA sequencing [RNA-seq]) hypothesis that low MARK4 levels correlated with TAU (Ser-262) hypo-phosphorylation could also contribute to MT stabilization (Figures 2C4 and 2D4), but it remains unclear whether the down-regulation of MARK4 is mediated by a mechanosensitive protein, a calcium-dependent protein, or other mechanisms.

A very interesting open issue is how a force of a few picoNewtons generated by nano-pulling can modulate the net contractile force resulting from the pulling forces generated by the GC and the axon shaft, which is hundreds of picoNewtons.[84] Here we propose a mechanism defined as "the axonal positive loop," according to which application of a force of a few picoNewtons to the axon triggers accumulation of MTs, each of them generating a force in the range of 4 pN,[85] and together they can decrease the pulling force generated by the axon onto the GC by hundreds of picoNewtons, pushing the tip forward. This mechanism is consistent with the observation that stretch growth occurs when axons are stretched from the soma to the tip but not from the tip to the soma.[22] This is due to the polarity of MTs, which, in stage 3 axons, have a preferential polarity with the plus end facing the tip.[86] More evidence of the connection between MT stabilization and axon elongation is that impairment of MT polymerization via nocodazole administration was found to totally block stretch growth,[25] probably by limiting the addition of new mass. When knocking out $\alpha$-tubulin or $\beta$-tubulin in touch receptor neurons of *C. elegans*, we found that stretch growth is not permitted (Figures 2B1 and 2B2). Stretch growth appears to be well conserved across evolution and strictly dependent on MT dynamics.

One of the most intriguing questions is how stabilization of MTs can be linked to the role of mechanical tension in mass addition. The GO analysis revealed functional enrichment in some cellular components, such as mitochondria (GO:0005739) and the ER (GO:0005783) (Figure 1C). This may reflect the high energy demand and the lipid and protein hyper-production required to sustain stretch growth. The data collected in this study provide evidence of accumulation of mitochondria and ERs in stretched neurites (Figures 3A and 3B). The increase in MT density in the stretched group could account for the accumulation of mitochondria and ER cisternae, whose transport is mostly dependent on MT-based motors.[87,88] MT stability was also found to influence the distribution and structural organization of the axonal ER.[88] MTs also represent the "tracks" on which vesicles move along the axon.[4] the most important result from the GOEA is related to vesicle processes, such as lysosome (GO:0005764), endosome (GO:0005768), LE (GO:0005770), and synaptic vesicle cycle (GO:0099504). By investigating some vesicular components, we found that nano-pulling promotes accumulation of synaptic vesicles (Figure 6) and signaling vesicles (Figure 3C). Accumulation of organelles and vesicles could result from accumulation of MTs, given that many of these components have an active motion on MTs.[41] However, another mechanism that needs to be considered is that force has been shown to modulate the unbinding rate

of molecular motors from MTs.[89] According to the "tug-of-war" model, a differential response of the kinesin and dynein molecular motors to the force could account for the modulation of vesicle transport.[90] An opposing force of a few picoNewtons causes the dynein to walk backwards toward the MT plus end.[91] It would be interesting in future works to investigate whether this force dependent behavior could explain our observation that the accumulation of NGF-vesicles is related to a decrease in the RET component rather than to an increase in the ANT one. Another possibility is that magnetic nano-pulling impairs the RET movement of MNP-labeled vesicles,[92] but we do not have evidence of accumulation of MNPs within vesicles. Here we took advantage of *C. elegans* to validate the hypothesis that the MT stabilization induced by nano-pulling is responsible for vesicle accumulation. We tracked UNC-104, a motor protein involved in MT-associated ANT vesicular transport and a marker for synaptic/dense core vesicles (synapsin SNN-1$^{+}$).[93] As expected, we found that stretch growth induces accumulation of UNC-104 in neurites (Figure 4A) and a corresponding accumulation of SNN-1 that was more pronounced in the GC (Figure 4D), where SNN-1 vesicles preferentially anchor.[61] However, impairment of MT stabilization via nocodazole treatment abolished UNC-104 accumulation (Figure 4B) and, consequently, stretch growth (Figure S3). Similarly, in the $\alpha$-tubulin mutant strain, there was no accumulation of SNN-1 at the tip (Figure 4E). The stabilization of MTs induced by nano-pulling is required for accumulation of UNC-104 motor proteins and its interacting vesicles (SNN-1$^{+}$). Consistent with previous data, treatment of hippocampal neurons with BFA, a global inhibitor of vesicle trafficking, resulted in a statistically significant reduction of stretch growth (Figure 3D).

The model that emerges from this study is that nano-pulling can stimulate accumulation in the axon of some components (organelles and vesicles) of the "translation platforms." When mitochondria accumulate in the axon shaft, they have a higher probability of associating with RNA granules and of activating local translation.[67] ER tubules that accumulate in stretched axons may also interact with many elements of the translational platforms, such as endosomes and mitochondria, to co-regulate this process.[94] Similarly, LEs are transported along the MT tracks through molecular motors,[95] and the link between the dynamics of axonal transport and MTs is very strong.[96] The increase in actively translating ribosomes (Figures 5B2–5B4), but not total ones (Figure 5C4), together with the increase in the functional interactions between LEs and RNA granules (Figure 5D3) and between LEs and active ribosomes (Figure 5D4) highlights that nano-pulling promotes local translation. We speculate that the increase in mitochondria and vesicle density in the axon shaft during nano-pulling increases the probability of formation of functional platforms for local translation. The view that activation of local translation in axons is necessary to sustain stretch growth is also consistent with the fact that inhibition of protein synthesis via CH treatment led to inhibition of stretch growth but not tip growth.[25] Treatment with CH resulted in blockage of stretch growth without changing MT density in stretched axons (Figure 5A), suggesting that activation of protein translation is downstream of MT stabilization.

Our data support the idea that application of active forces on axons promotes creation of a complex dialog between axonal transport and local translation and that this dialog may be driven by MTs. According to the model proposed here, nano-pulling promotes stabilization of MTs, which modulates axonal transport, resulting in accumulation of organelles and vesicles in the axon and facilitating assembly of the translation platforms that stimulate activation of local translation. This cross-talk could be responsible for the supply of vesicles, lipids, and proteins required for sustaining axon outgrowth (Figure 1A2) and synaptic maturation (Figures 6 and 7).

### Limitations of the study

A limitation of the present study is that the force generated by magnetic nano-pulling has been estimated, but a direct measure of the applied force is missing. We identified that the MTs have a hub of signal transduction, but the mechanosensitive element was not clarified. More studies are needed to elucidate the complete signaling cascade and the principles of mechanosensing. It will be imperative to validate the proposed model *in vivo*, under physiological conditions, where axons that are synaptically connected are under mechanical tension.

## STAR★METHODS

Detailed methods are provided in the online version of this paper and include the following:

- KEY RESOURCES TABLE
- RESOURCE AVAILABILITY
  - Lead contact
  - Materials availability
  - Data and code availability
- EXPERIMENTAL MODEL AND SUBJECT DETAILS
  - Mice
  - *C. elegans*
- METHOD DETAILS
  - Cell culture
  - Drug treatment
  - Nanoparticles
  - Microfluidic chambers
  - Magnetic nano-pulling assay
  - RNA extraction and quantification
  - RNA sequencing
  - Quality check at the biological and bioinformatic level
  - GO and GOEA
  - Ribopuromycylation
  - Immunostaining and imaging
  - Sample preparation for TEM
  - NGF single vesicle tracking
- QUANTIFICATION AND STATISTICAL ANALYSIS
  - Image analysis
  - TEM analysis
  - Statistical analysis

## SUPPLEMENTAL INFORMATION

Supplemental information can be found online at https://doi.org/10.1016/j.celrep.2022.111912.

## ACKNOWLEDGMENTS

The study was supported by the Wings for Life Foundation (WFL-IT-16/17 and 20/21), the Italian Ministry of Economical Development through the MAECI (MagNerv), the ERC (MechanoSystems, 715243), the HFSP (CDA00023/2018 and RGP0026/2021), the Spanish Ministry of Economy and Competitiveness (PID2021-123812OB-I00 project funded by MCIN /AEI /10.13039/501100011033 / FEDER, UE), the "Severo Ochoa" program for Centres of Excellence in R\&D (CEX2019-000910-S), Ramon-y-Cajal Program (RYC-2016-21062), the Fundació Privada Cellex, Fundació Mir-Puig, and Generalitat de Catalunya through the CERCA and research program (2017 SGR 1012). We thank the NMSB lab for discussions, Nawaphat Malaiwong for help with *C. elegans* cell culture, and M. Harterink (University of Utrecht) for sharing unpublished reagents. We thank Alessandra Galeotti for the transcriptomics data, Pietro Folino for re-analyzing data related pharmacological treatments, and Antonino Cattaneo and Antonietta Calvello of the Bio@SNS lab for making NGF-YBBR available for this study.

## AUTHOR CONTRIBUTIONS

Conceptualization, M.K. and V.R.; methodology, A.F., V.C., L.M., S.L., F.-C.C., and R.D.; formal analysis, U.B.; investigation, A.F., S.D.V., V.C., D.C., S.G., and S.F.; writing – original draft, V.R. and A.F.; writing – review & editing, all authors; funding acquisition, M.K. and V.R.; resources, V.C., S.L., L.M., M.K., and V.R.; supervision, L.M., U.B., M.K., and V.R.

## DECLARATION OF INTERESTS

The authors declare no competing interests.

Received: April 6, 2022
Revised: November 16, 2022
Accepted: December 12, 2022

## REFERENCES

1. Franze, K. (2013). The mechanical control of nervous system development. Development *140*, 3069–3077.
2. Suter, D.M., and Miller, K.E. (2011). The emerging role of forces in axonal elongation. Prog. Neurobiol. *94*, 91–101. https://doi.org/10.1016/j.pneurobio.2011.04.002.
3. Tamariz, E., and Varela-Echavarría, A. (2015). The discovery of the growth cone and its influence on the study of axon guidance. Front. Neuroanat. *9*, 51.
4. Lowery, L.A., and Van Vactor, D. (2009). The trip of the tip: understanding the growth cone machinery. Nat. Rev. Mol. Cell Biol. *10*, 332–343.
5. Lee, A.C., and Suter, D.M. (2008). Quantitative analysis of microtubule dynamics during adhesion-mediated growth cone guidance. Dev. Neurobiol. *68*, 1363–1377.
6. Toriyama, M., Kozawa, S., Sakumura, Y., and Inagaki, N. (2013). Conversion of a signal into forces for axon outgrowth through Pak1-mediated shootin1 phosphorylation. Curr. Biol. *23*, 529–534.
7. Turney, S.G., Ahmed, M., Chandrasekar, I., Wysolmerski, R.B., Goeckeler, Z.M., Rioux, R.M., Whitesides, G.M., and Bridgman, P.C. (2016). Nerve growth factor stimulates axon outgrowth through negative regulation of growth cone actomyosin restraint of microtubule advance. Mol. Biol. Cell *27*, 500–517.
8. de Rooij, R., Kuhl, E., and Miller, K.E. (2018). Modeling the axon as an active partner with the growth cone in axonal elongation. Biophys. J. *115*, 1783–1795.
9. Weiss, P., and Hiscoe, H.B. (1948). Experiments on the mechanism of nerve growth. J. Exp. Zool. *107*, 315–395.
10. Marsh, L., and Letourneau, P.C. (1984). Growth of neurites without filopodial or lamellipodial activity in the presence of cytochalasin B. J. Cell Biol. *99*, 2041–2047.
11. Pfister, B.J., Iwata, A., Meaney, D.F., and Smith, D.H. (2004). Extreme stretch growth of integrated axons. J. Neurosci. *24*, 7978–7983.
12. Magdesian, M.H., Lopez-Ayon, G.M., Mori, M., Boudreau, D., Goulet-Hanssens, A., Sanz, R., Miyahara, Y., Barrett, C.J., Fournier, A.E., De Koninck, Y., and Grütter, P. (2016). Rapid mechanically controlled rewiring of neuronal circuits. J. Neurosci. *36*, 979–987.
13. Lamoureux, P., Buxbaum, R.E., and Heidemann, S.R. (1989). Direct evidence that growth cones pull. Nature *340*, 159–162.
14. Steketee, M.B., Oboudiyat, C., Daneman, R., Trakhtenberg, E., Lamoureux, P., Weinstein, J.E., Heidemann, S., Barres, B.A., and Goldberg, J.L. (2014). Regulation of intrinsic axon growth ability at retinal ganglion cell growth cones. Invest. Ophthalmol. Vis. Sci. *55*, 4369–4377.
15. Bray, D. (1984). Axonal growth in response to experimentally applied mechanical tension. Dev. Biol. *102*, 379–389.
16. Lamoureux, P., Heidemann, S.R., Martzke, N.R., and Miller, K.E. (2010). Growth and elongation within and along the axon. Dev. Neurobiol. *70*, 135–149.
17. Miller, K.E., and Sheetz, M.P. (2006). Direct evidence for coherent low velocity axonal transport of mitochondria. J. Cell Biol. *173*, 373–381.
18. Chowdary, P.C., McGuire, A., Lee, Y., Che, D., Hanson, L., Osakada, Y., Ooi, C., Xie, C., Wang, S.X., and Cui, B. (2019). Magnetic manipulation of axonal endosome transport in live neurons. Preprint at bioRxiv. https://doi.org/10.1101/733253.
19. Gahl, T.J., and Kunze, A. (2018). Force-mediating magnetic nanoparticles to engineer neuronal cell function. Front. Neurosci. *12*, 299.
20. Kunze, A., Tseng, P., Godzich, C., Murray, C., Caputo, A., Schweizer, F.E., and Di Carlo, D. (2015). Engineering cortical neuron polarity with nanomagnets on a chip. ACS Nano *9*, 3664–3676.
21. Kunze, A., Murray, C.T., Godzich, C., Lin, J., Owsley, K., Tay, A., and Di Carlo, D. (2017). Modulating motility of intracellular vesicles in cortical neurons with nanomagnetic forces on-chip. Lab Chip *17*, 842–854.
22. Raffa, V., Falcone, F., De Vincentiis, S., Falconieri, A., Calatayud, M.P., Goya, G.F., and Cuschieri, A. (2018). Piconewton mechanical forces promote neurite growth. Biophys. J. *115*, 2026–2033.
23. Riggio, C., Calatayud, M.P., Giannaccini, M., Sanz, B., Torres, T.E., Fernández-Pacheco, R., Ripoli, A., Ibarra, M.R., Dente, L., Cuschieri, A., et al. (2014). The orientation of the neuronal growth process can be directed via magnetic nanoparticles under an applied magnetic field. Nanomedicine *10*, 1549–1558.
24. Tay, A., Kunze, A., Murray, C., and Di Carlo, D. (2016). Induction of calcium influx in cortical neural networks by nanomagnetic forces. ACS Nano *10*, 2331–2341.
25. De Vincentiis, S., Falconieri, A., Mainardi, M., Cappello, V., Scribano, V., Bizzarri, R., Storti, B., Dente, L., Costa, M., and Raffa, V. (2020). Extremely low forces induce extreme axon growth. J. Neurosci. *40*, 4997–5007.
26. Wang, Y., Li, B., Xu, H., Du, S., Liu, T., Ren, J., Zhang, J., Zhang, H., Liu, Y., and Lu, L. (2020). Growth and elongation of axons through mechanical tension mediated by fluorescent-magnetic bifunctional Fe 3 O 4· Rhodamine 6G@ PDA superparticles. J. Nanobiotechnol. *18*. 64–18.
27. Chowdary, P.D., Xie, C., Osakada, Y., Che, D.L., and Cui, B. (2013). Magnetic manipulation of axonal transport in live neurons. Biophys. J. *104*, 652a.
28. Dai, R., Hang, Y., Liu, Q., Zhang, S., Wang, L., Pan, Y., and Chen, H. (2019). Improved neural differentiation of stem cells mediated by magnetic nanoparticle-based biophysical stimulation. J. Mater. Chem. B *7*, 4161–4168.
29. Kim, H.J., Byun, J.H., Park, J.W., Vahidi, B., Rhee, S.W., Jeon, N.L., and Jeon, N.L. (2012). Integrated microfluidics platforms for investigating injury and regeneration of CNS axons. Ann. Biomed. Eng. *40*, 1268–1276.
30. Taylor, A.M., Blurton-Jones, M., Rhee, S.W., Cribbs, D.H., Cotman, C.W., and Jeon, N.L. (2005). A microfluidic culture platform for CNS axonal injury, regeneration and transport. Nat. Methods *2*, 599–605.

31. Nijssen, J., Aguila, J., Hoogstraaten, R., Kee, N., and Hedlund, E. (2018). Axon-seq decodes the motor axon transcriptome and its modulation in response to ALS. Stem Cell Rep. *11*, 1565–1578.

32. Huang, D.W., Sherman, B.T., and Lempicki, R.A. (2009). Systematic and integrative analysis of large gene lists using DAVID bioinformatics resources. Nat. Protoc. *4*, 44–57.

33. Koopmans, F., van Nierop, P., Andres-Alonso, M., Byrnes, A., Cijsouw, T., Coba, M.P., Cornelisse, L.N., Farrell, R.J., Goldschmidt, H.L., Howrigan, D.P., et al. (2019). SynGO: an evidence-based, expert-curated knowledge base for the synapse. Neuron *103*, 217–234.e4.

34. Witte, H., Neukirchen, D., and Bradke, F. (2008). Microtubule stabilization specifies initial neuronal polarization. J. Cell Biol. *180*, 619–632.

35. Fukushige, T., Siddiqui, Z.K., Chou, M., Culotti, J.G., Gogonea, C.B., Siddiqui, S.S., and Hamelin, M. (1999). MEC-12, an alpha-tubulin required for touch sensitivity in C. elegans. J. Cell Sci. *112*, 395–403.

36. Lockhead, D., Schwarz, E.M., O'Hagan, R., Bellotti, S., Krieg, M., Barr, M.M., Dunn, A.R., Sternberg, P.W., and Goodman, M.B. (2016). The tubulin repertoire of Caenorhabditis elegans sensory neurons and its context-dependent role in process outgrowth. Mol. Biol. Cell *27*, 3717–3728.

37. Zheng, C., Diaz-Cuadros, M., Nguyen, K.C.Q., Hall, D.H., and Chalfie, M. (2017). Distinct effects of tubulin isotype mutations on neurite growth in Caenorhabditis elegans. Mol. Biol. Cell *28*, 2786–2801.

38. Li, G., and Moore, J.K. (2020). Microtubule dynamics at low temperature: evidence that tubulin recycling limits assembly. Mol. Biol. Cell *31*, 1154–1166.

39. Goedert, M., Baur, C.P., Ahringer, J., Jakes, R., Hasegawa, M., Spillantini, M.G., Smith, M.J., and Hill, F. (1996). PTL-1, a microtubule-associated protein with tau-like repeats from the nematode Caenorhabditis elegans. J. Cell Sci. *109*, 2661–2672.

40. Krieg, M., Stühmer, J., Cueva, J.G., Fetter, R., Spilker, K., Cremers, D., Shen, K., Dunn, A.R., and Goodman, M.B. (2017). Genetic defects in β-spectrin and tau sensitize C. elegans axons to movement-induced damage via torque-tension coupling. Elife *6*, e20172.

41. Sánchez-Huertas, C., and Herrera, E. (2021). With the permission of microtubules: an updated overview on microtubule function during axon pathfinding. Front. Mol. Neurosci. *14*, 759404.

42. Trushko, A., Schäffer, E., and Howard, J. (2013). The growth speed of microtubules with XMAP215-coated beads coupled to their ends is increased by tensile force. Proc. Natl. Acad. Sci. USA *110*, 14670–14675.

43. Kadavath, H., Hofele, R.V., Biernat, J., Kumar, S., Tepper, K., Urlaub, H., Mandelkow, E., and Zweckstetter, M. (2015). Tau stabilizes microtubules by binding at the interface between tubulin heterodimers. Proc. Natl. Acad. Sci. USA *112*, 7501–7506.

44. Biernat, J., Gustke, N., Drewes, G., Mandelkow, E.M., and Mandelkow, E. (1993). Phosphorylation of Ser262 strongly reduces binding of tau to microtubules: distinction between PHF-like immunoreactivity and microtubule binding. Neuron *11*, 153–163.

45. Oba, T., Saito, T., Asada, A., Shimizu, S., Iijima, K.M., and Ando, K. (2020). Microtubule affinity–regulating kinase 4 with an Alzheimer's disease-related mutation promotes tau accumulation and exacerbates neurodegeneration. J. Biol. Chem. *295*, 17138–17147.

46. Sengupta, A., Kabat, J., Novak, M., Wu, Q., Grundke-Iqbal, I., and Iqbal, K. (1998). Phosphorylation of tau at both Thr 231 and Ser 262 is required for maximal inhibition of its binding to microtubules. Arch. Biochem. Biophys. *357*, 299–309.

47. Lindwall, G., and Cole, R.D. (1984). Phosphorylation affects the ability of tau protein to promote microtubule assembly. J. Biol. Chem. *259*, 5301–5305.

48. Liu, F., Li, B., Tung, E.J., Grundke-Iqbal, I., Iqbal, K., and Gong, C.X. (2007). Site-specific effects of tau phosphorylation on its microtubule assembly activity and self-aggregation. Eur. J. Neurosci. *26*, 3429–3436.

49. Scott, C.W., Spreen, R.C., Herman, J.L., Chow, F.P., Davison, M.D., Young, J., and Caputo, C.B. (1993). Phosphorylation of recombinant tau by cAMP-dependent protein kinase. Identification of phosphorylation sites and effect on microtubule assembly. J. Biol. Chem. *268*, 1166–1173.

50. Falleroni, F., Bocchero, U., Mortal, S., Li, Y., Ye, Z., Cojoc, D., and Torre, V. (2022). Mechanotransduction in hippocampal neurons operates under localized low picoNewton forces. iScience *25*, 103807.

51. Shen, X., Song, Z., Xu, E., Zhou, J., and Yan, F. (2021). Sensitization of nerve cells to ultrasound stimulation through Piezo1-targeted microbubbles. Ultrason. Sonochem. *73*, 105494.

52. Lim, J., Tai, H.-H., Liao, W.-H., Chu, Y.-C., Hao, C.-M., Huang, Y.-C., Lee, C.-H., Lin, S.-S., Hsu, S., Chien, Y.-C., et al. (2021). ASIC1a is required for neuronal activation via low-intensity ultrasound stimulation in mouse brain. Elife *10*, e61660.

53. Sumi, T., Yamamoto, H., and Hirano-Iwata, A. (2020). Suppression of hypersynchronous network activity in cultured cortical neurons using an ultrasoft silicone scaffold. Soft Matter *16*, 3195–3202.

54. O'Hagan, R., Chalfie, M., and Goodman, M.B. (2005). The MEC-4 DEG/ENaC channel of Caenorhabditis elegans touch receptor neurons transduces mechanical signals. Nat. Neurosci. *8*, 43–50.

55. Howe, C.L., and Mobley, W.C. (2004). Signaling endosome hypothesis: a cellular mechanism for long distance communication. J. Neurobiol. *58*, 207–216.

56. Convertino, D., Fabbri, F., Mishra, N., Mainardi, M., Cappello, V., Testa, G., Capsoni, S., Albertazzi, L., Luin, S., Marchetti, L., and Coletti, C. (2020). Graphene promotes axon elongation through local stall of Nerve Growth Factor signaling endosomes. Nano Lett. *20*, 3633–3641.

57. Jareb, M., and Banker, G. (1997). Inhibition of axonal growth by brefeldin A in hippocampal neurons in culture. J. Neurosci. *17*, 8955–8963.

58. Wisco, D., Anderson, E.D., Chang, M.C., Norden, C., Boiko, T., Fölsch, H., and Winckler, B. (2003). Uncovering multiple axonal targeting pathways in hippocampal neurons. J. Cell Biol. *162*, 1317–1328.

59. Hall, D.H., and Hedgecock, E.M. (1991). Kinesin-related gene unc-104 is required for axonal transport of synaptic vesicles in C. elegans. Cell *65*, 837–847.

60. Vasquez, R.J., Howell, B., Yvon, A.M., Wadsworth, P., and Cassimeris, L. (1997). Nanomolar concentrations of nocodazole alter microtubule dynamic instability in vivo and in vitro. Mol. Biol. Cell *8*, 973–985.

61. Bloom, O., Evergren, E., Tomilin, N., Kjaerulff, O., Löw, P., Brodin, L., Pieribone, V.A., Greengard, P., and Shupliakov, O. (2003). Colocalization of synapsin and actin during synaptic vesicle recycling. J. Cell Biol. *161*, 737–747.

62. Siegel, M.R., and Sisler, H.D. (1963). Inhibition of protein synthesis in vitro by cycloheximide. Nature *200*, 675–676.

63. Holt, C.E., Martin, K.C., and Schuman, E.M. (2019). Local translation in neurons: visualization and function. Nat. Struct. Mol. Biol. *26*, 557–566.

64. Nagano, S., and Araki, T. (2021). Axonal transport and local translation of mRNA in neurodegenerative diseases. Front. Mol. Neurosci. *14*, 697973.

65. Nagano, S., Jinno, J., Abdelhamid, R.F., Jin, Y., Shibata, M., Watanabe, S., Hirokawa, S., Nishizawa, M., Sakimura, K., Onodera, O., et al. (2020). TDP-43 transports ribosomal protein mRNA to regulate axonal local translation in neuronal axons. Acta Neuropathol. *140*, 695–713.

66. Shigeoka, T., Koppers, M., Wong, H.H.-W., Lin, J.Q., Cagnetta, R., Dwivedy, A., de Freitas Nascimento, J., van Tartwijk, F.W., Ströhl, F., Cioni, J.-M., et al. (2019). On-site ribosome remodeling by locally synthesized ribosomal proteins in axons. Cell Rep. *29*, 3605–3619.e10.

67. Cioni, J.-M., Lin, J.Q., Holtermann, A.V., Koppers, M., Jakobs, M.A.H., Azizi, A., Turner-Bridger, B., Shigeoka, T., Franze, K., Harris, W.A., and Holt, C.E. (2019). Late endosomes act as mRNA translation platforms and sustain mitochondria in axons. Cell *176*, 56–72.e15.

68. Liao, Y.-C., Fernandopulle, M.S., Wang, G., Choi, H., Hao, L., Drerup, C.M., Patel, R., Qamar, S., Nixon-Abell, J., Shen, Y., et al. (2019). RNA

granules hitchhike on lysosomes for long-distance transport, using annexin A11 as a molecular tether. Cell *179*, 147–164.e20.

69. Spillane, M., Ketschek, A., Merianda, T.T., Twiss, J.L., and Gallo, G. (2013). Mitochondria coordinate sites of axon branching through localized intra-axonal protein synthesis. Cell Rep. *5*, 1564–1575.
70. Gitler, D., Takagishi, Y., Feng, J., Ren, Y., Rodriguiz, R.M., Wetsel, W.C., Greengard, P., and Augustine, G.J. (2004). Different presynaptic roles of synapsins at excitatory and inhibitory synapses. J. Neurosci. *24*, 11368–11380.
71. Muller, D., Buchs, P.-A., and Stoppini, L. (1993). Time course of synaptic development in hippocampal organotypic cultures. Brain Res. Dev. Brain Res. *71*, 93–100.
72. Liu, Y.-T., Tao, C.-L., Lau, P.-M., Zhou, Z.H., and Bi, G.-Q. (2019). Postsynaptic protein organization revealed by electron microscopy. Curr. Opin. Struct. Biol. *54*, 152–160.
73. Zhang, W., and Benson, D.L. (2001). Stages of synapse development defined by dependence on F-actin. J. Neurosci. *21*, 5169–5181.
74. Gürth, C.-M., Dankovich, T.M., Rizzoli, S.O., and D'Este, E. (2020). Synaptic activity and strength are reflected by changes in the post-synaptic secretory pathway. Sci. Rep. *10*, 1–13.
75. Gangatharan, G., Schneider-Maunoury, S., and Breau, M.A. (2018). Role of mechanical cues in shaping neuronal morphology and connectivity. Biol. Cell *110*, 125–136.
76. Krieg, M., Dunn, A.R., and Goodman, M.B. (2014). Mechanical control of the sense of touch by β-spectrin. Nat. Cell Biol. *16*, 224–233.
77. Miller, K.E., and Suter, D.M. (2018). An integrated cytoskeletal model of neurite outgrowth. Front. Cell. Neurosci. *12*, 447.
78. Falconieri, A., Taparia, N., De Vincentiis, S., Cappello, V., Sniadecki, N.J., and Raffa, V. (2022). Magnetically-actuated microposts stimulate axon growth. Biophys. J. *121*, 374–382.
79. Hamant, O., Inoue, D., Bouchez, D., Dumais, J., and Mjolsness, E. (2019). Are microtubules tension sensors? Nat. Commun. *10*, 2360.
80. Inoue, D., Nitta, T., Kabir, A.M.R., Sada, K., Gong, J.P., Konagaya, A., and Kakugo, A. (2016). Sensing surface mechanical deformation using active probes driven by motor proteins. Nat. Commun. *7*, 12557.
81. Akiyoshi, B., Sarangapani, K.K., Powers, A.F., Nelson, C.R., Reichow, S.L., Arellano-Santoyo, H., Gonen, T., Ranish, J.A., Asbury, C.L., and Biggins, S. (2010). Tension directly stabilizes reconstituted kinetochore-microtubule attachments. Nature *468*, 576–579.
82. Putnam, A.J., Schultz, K., and Mooney, D.J. (2001). Control of microtubule assembly by extracellular matrix and externally applied strain. Am. J. Physiol. Cell Physiol. *280*, C556–C564.
83. Franck, A.D., Powers, A.F., Gestaut, D.R., Gonen, T., Davis, T.N., and Asbury, C.L. (2007). Tension applied through the Dam1 complex promotes microtubule elongation providing a direct mechanism for length control in mitosis. Nat. Cell Biol. *9*, 832–837.
84. O'Toole, M., Lamoureux, P., and Miller, K.E. (2015). Measurement of subcellular force generation in neurons. Biophys. J. *108*, 1027–1037.
85. Kolomeisky, A.B., and Fisher, M.E. (2001). Force-velocity relation for growing microtubules. Biophys. J. *80*, 149–154.
86. Yogev, S., and Shen, K. (2017). Establishing neuronal polarity with environmental and intrinsic mechanisms. Neuron *96*, 638–650.
87. Lin, M.-Y., and Sheng, Z.-H. (2015). Regulation of mitochondrial transport in neurons. Exp. Cell Res. *334*, 35–44.
88. Farías, G.G., Fréal, A., Tortosa, E., Stucchi, R., Pan, X., Portegies, S., Will, L., Altelaar, M., and Hoogenraad, C.C. (2019). Feedback-driven mechanisms between microtubules and the endoplasmic reticulum instruct neuronal polarity. Neuron *102*, 184–201.e8.
89. Berger, F., Klumpp, S., and Lipowsky, R. (2019). Force-dependent unbinding rate of molecular motors from stationary optical trap data. Nano Lett. *19*, 2598–2602.
90. Leidel, C., Longoria, R.A., Gutierrez, F.M., and Shubeita, G.T. (2012). Measuring molecular motor forces in vivo: implications for tug-of-war models of bidirectional transport. Biophys. J. *103*, 492–500.
91. Gennerich, A., Carter, A.P., Reck-Peterson, S.L., and Vale, R.D. (2007). Force-induced bidirectional stepping of cytoplasmic dynein. Cell *131*, 952–965.
92. Steketee, M.B., Moysidis, S.N., Jin, X.-L., Weinstein, J.E., Pita-Thomas, W., Raju, H.B., Iqbal, S., and Goldberg, J.L. (2011). Nanoparticle-mediated signaling endosome localization regulates growth cone motility and neurite growth. Proc. Natl. Acad. Sci. USA *108*, 19042–19047.
93. Patel, M.R., Lehrman, E.K., Poon, V.Y., Crump, J.G., Zhen, M., Bargmann, C.I., and Shen, K. (2006). Hierarchical assembly of presynaptic components in defined C. elegans synapses. Nat. Neurosci. *9*, 1488–1498.
94. Merianda, T.T., Lin, A.C., Lam, J.S.Y., Vuppalanchi, D., Willis, D.E., Karin, N., Holt, C.E., and Twiss, J.L. (2009). A functional equivalent of endoplasmic reticulum and Golgi in axons for secretion of locally synthesized proteins. Mol. Cell. Neurosci. *40*, 128–142.
95. Welte, M.A. (2004). Bidirectional transport along microtubules. Curr. Biol. *14*, R525–R537.
96. Yogev, S., Cooper, R., Fetter, R., Horowitz, M., and Shen, K. (2016). Microtubule organization determines axonal transport dynamics. Neuron *92*, 449–460.
97. Di Matteo, P., Calvello, M., Luin, S., Marchetti, L., and Cattaneo, A. (2017). An optimized procedure for the site-directed labeling of NGF and proNGF for imaging purposes. Front. Mol. Biosci. *4*, 4.
98. Gobbo, F., Bonsignore, F., Amodeo, R., Cattaneo, A., and Marchetti, L. (2018). Site-specific direct labeling of neurotrophins and their receptors: from biochemistry to advanced imaging applications. In Neurotrophic Factors (Springer), pp. 295–314.
99. Nekimken, A.L., Fehlauer, H., Kim, A.A., Manosalvas-Kjono, S.N., Ladpli, P., Memon, F., Gopisetty, D., Sanchez, V., Goodman, M.B., Pruitt, B.L., and Krieg, M. (2017). Pneumatic stimulation of C. elegans mechanoreceptor neurons in a microfluidic trap. Lab Chip *17*, 1116–1127.
100. Wen, Q., Po, M.D., Hulme, E., Chen, S., Liu, X., Kwok, S.W., Gershow, M., Leifer, A.M., Butler, V., Fang-Yen, C., et al. (2012). Proprioceptive coupling within motor neurons drives C. elegans forward locomotion. Neuron *76*, 750–761.
101. Schneider, C.A., Rasband, W.S., and Eliceiri, K.W. (2012). NIH Image to ImageJ: 25 years of image analysis. Nat. Methods *9*, 671–675.
102. Ippolito, D.M., and Eroglu, C. (2010). Quantifying synapses: an immunocytochemistry-based assay to quantify synapse number. J. Vis. Exp., e2270.
103. Meijering, E., Jacob, M., Sarria, J.C.F., Steiner, P., Hirling, H., and Unser, M. (2004). Design and validation of a tool for neurite tracing and analysis in fluorescence microscopy images. Cytometry A. *58*, 167–176.
104. Gilles, J.-F., Dos Santos, M., Boudier, T., Bolte, S., and Heck, N. (2017). DiAna, an ImageJ tool for object-based 3D co-localization and distance analysis. Methods *115*, 55–64.
105. Harterink, M., van Bergeijk, P., Allier, C., de Haan, B., van den Heuvel, S., Hoogenraad, C.C., and Kapitein, L.C. (2016). Light-controlled intracellular transport in Caenorhabditis elegans. Curr. Biol. *26*, R153–R154.
106. Das, R., Lin, L.C., Català-Castro, F., Malaiwong, N., Sanfeliu-Cerdán, N., Porta-de-la-Riva, M., et al. (2021). An asymmetric mechanical code ciphers curvature-dependent proprioceptor activity. Sci. Adv. *7*, eabg4617.
107. Mills, R., Taylor-Weiner, H., Correia, J.C., Agudelo, L.Z., Allodi, I., Kolonelou, C., Martinez-Redondo, V., Ferreira, D.M.S., Nichterwitz, S., Comley, L.H., et al. (2018). Neurturin is a PGC-1α1-controlled myokine that promotes motor neuron recruitment and neuromuscular junction formation. Mol. Metab. *7*, 12–22.

108. Bastide, A., Yewdell, J.W., and David, A. (2018). The RiboPuromycylation method (RPM): an immunofluorescence technique to map translation sites at the sub-cellular level. Bio. Protoc. *8*, e2669.

109. Moscardini, A., Di Pietro, S., Signore, G., Parlanti, P., Santi, M., Gemmi, M., and Cappello, V. (2020). Uranium-free X solution: a new generation contrast agent for biological samples ultrastructure. Sci. Rep. *10*, 11540.

110. Yin, J., Straight, P.D., McLoughlin, S.M., Zhou, Z., Lin, A.J., Golan, D.E., Kelleher, N.L., Kolter, R., and Walsh, C.T. (2005). Genetically encoded short peptide tag for versatile protein labeling by Sfp phosphopantetheinyl transferase. Proc. Natl. Acad. Sci. USA *102*, 15815–15820.

111. Amodeo, R., Convertino, D., Calvello, M., Ceccarelli, L., Bonsignore, F., Ravelli, C., Cattaneo, A., Martini, C., Luin, S., Mitola, S., et al. (2020). Fluorolabeling of the PPTase-related chemical tags: comparative study of different membrane receptors and different fluorophores in the labeling reactions. Front. Mol. Biosci. *7*, 195.

## STAR★METHODS

### KEY RESOURCES TABLE

| REAGENT or RESOURCE | SOURCE | IDENTIFIER |
|---|---|---|
| Antibodies | | |
| Mouse monoclonal anti-TUBB3 | Sigma-Aldrich | #T8578 RRID:AB_1841228 |
| Rabbit polyclonal anti-Synapsin I | Synaptic Systems | #106 103 RRID:AB_11042000 |
| Rabbit polyclonal anti-Homer 1b/c | Synaptic Systems | #160 023 RRID:AB_2619858 |
| Mouse monoclonal anti-VGlut1 | Sigma-Aldrich | # AMAB91041 RRID:AB_2665777 |
| Rabbit monoclonal anti-S6 | Cell signaling | #2217 RRID:AB_331355 |
| Rabbit polyclonal anti-Mark4 | Abcam | # ab124267 RRID:AB_10999863 |
| Rabbit polyclonal anti-Tau (p-Ser262) | Abcam | # ab131354 RRID:AB_11156689 |
| Chicken polyclonal anti-TUBB3 | Abcam | #ab41489 RRID:AB_727049 |
| Rabbit polyclonal anti-Rab7 | Abcam | #ab137029 RRID:AB_2629474 |
| Mouse monoclonal anti-Puromycin | Sigma-Aldrich | #MABE343 RRID:AB_2566826 |
| Goat polyclonal anti-Mouse, Oregon Green 488 | Thermo Fisher Scientific | #O6380 RRID:AB_1500662 |
| Goat polyclonal anti-Rabbit, Alexa Fluor Plus 488 | Thermo Fisher Scientific | #A32731 RRID:AB_2633280 |
| Goat polyclonal anti-Rabbit, Alexa Fluor 568 | Thermo Fisher Scientific | #A11011 RRID:AB_143157 |
| Goat polyclonal anti-Mouse, Alexa Fluor Plus 647 | Thermo Fisher Scientific | #A32728 RRID:AB_2633277 |
| Goat polyclonal anti-Mouse, Rhodamine Red-X | Thermo Fisher Scientific | #R6393 RRID:AB_1500645 |
| Goat polyclonal anti-Chicken, Alexa Fluor 647 | Thermo Fisher Scientific | #A21449 RRID:AB_1500594 |
| Goat polyclonal anti-Chicken, Alexa Fluor 488 | Abcam | # ab150169 RRID:AB_2636803 |
| acetylated tubulin | Sigma-Aldrich | #T7451 RRID:AB_609894 |
| tyrosinated tubulin | Abcam | # ab6160 RRID:AB_305328 |
| Chemicals, peptides, and recombinant proteins | | |
| poly-L-lysine | Sigma-Aldrich | #P4707 |
| Laminin | Sigma-Aldrich | #L2020 |
| AraC | Sigma-Aldrich | #C1768 |
| collagenase from Clostridium histolyticum | Sigma-Aldrich | #C7657 |
| dispase II protease | Sigma-Aldrich | #D4693 |
| deoxyribonuclease I from bovine pancreas | Sigma-Aldrich | #DN25 |
| trypsin inhibitor from Glycine max | Sigma-Aldrich | #T9003 |
| Nerve growth factor | Sigma-Aldrich | #N5415 |
| poly-D-lysine | Sigma-Aldrich | #A-003-E |
| Chitinase | Sigma-Aldrich | #C6137 |
| Durapore filter | Millipore | #SVLP04700 |
| peanut lectin | Medicago | #05-0116-10 |
| emetine | Sigma-Aldrich | #E2375 |
| puromycin | Sigma-Aldrich | #P7255 |
| digitonin | Sigma-Aldrich | #D141 |
| Hoechst 33342 | Thermo Fisher Scientific | #H3570 |
| Syto RNA select | Thermo Fisher Scientific | #S32703 |
| nocodazole | Sigma-Aldrich | #SML1665 |
| brefaldin-A | Sigma-Aldrich | #B5936 |
| cycloexamide | Sigma-Aldrich | #C7698 |
| GsMTx-4 | Sigma-Aldrich | #SML3140 |
| YBBR-tagged NGF | recombinantly produced in *E. coli* | (di Matteo et al., 2017)[97] |
| CoA-Alexa647 | Produced in lab | (Gobbo et al., 2018)[98] |
| Sfp Synthase | Produced in lab | (Gobbo et al., 2018)[98] |

(*Continued on next page*)

*Continued*

| REAGENT or RESOURCE | SOURCE | IDENTIFIER |
|---|---|---|
| **Critical commercial assays** | | |
| NucleoSpin RNA PLUS XS Kit | Machery-Nagel | #740990.50 |
| Quant-iT RiboGreen RNA Kit | Thermo Fisher Scientific | US, #R11490 |
| QuantiTect Reverse Transcription Kit | Qiagen | #205311 |
| GoTaq®pPCR | Promega | #A6001 |
| Epoxy embedding medium kit | Merk KGaA | #45359-1EA-F |
| **Deposited data** | | |
| Axon-Seq, fastQ files | GEO | GSE197808 |
| **Experimental models: Organisms/strains** | | |
| Mouse: C57BL/6J | Charles River | 027C57BL/6 |
| *C. elegans* strain: GN692 [ljSi123[mec-7p: GCaMP6s::SL2::tagRFP]; lite-1(ce314)] | (Nekimken et al., 2017)[99] | N/A |
| *C. elegans* strain: GN693 [ljSi123[mec-7p: GCaMP6s::SL2::tagRFP]; lite-1(ce314); mec-4(u253)] | (Nekimken et al., 2017)[99] | N/A |
| *C. elegans* strain: MSB32 [hpIs258; lite-1(ce314) X] | (Wen et al., 2012)[100] | N/A |
| *C. elegans* strain: GN510 [mec-4(zdIs5) I; mec-12(e1607) III] | (Krieg et al., 2017)[40] | N/A |
| *C. elegans* strain: GN647 [ptl-1(pg73) III; mec-7(ok2152) X] | (Krieg et al., 2017)[40] | N/A |
| *C. elegans* strain: MSB1094[snn-1(syb2590); mec-4(zdIs5)I] | Michael Krieg's lab | N/A |
| *C. elegans* strain: MSB1095 [snn-1(syb2590); mec-4(zdIs5) I; mec-12(e1607) III] | Michael Krieg's lab | N/A |
| *C. elegans* strain: STR399[unc-119(ed3); hrtSi45[mec-4::unc-104pex::gfp::epdz LGI]] | Martin Harterink's lab | N/A |
| **Oligonucleotides** | | |
| Primer β-act Forward: AGCCATGTACGTAGCCATCC | Sigma-Aldrich | N/A |
| Primer β-act Reverse: CTCTCAGCTGTGGTGGTGAA | Sigma-Aldrich | N/A |
| Primer H1 Forward: AAAGCCACCCCTGTCAAGAA | Sigma-Aldrich | N/A |
| Primer H1 Reverse: CCTCTTGGCACTCGACTTGG | Sigma-Aldrich | N/A |
| **Software and algorithms** | | |
| FastQC v0.11.9 | https://www.bioinformatics.babraham.ac.uk/projects/fastqc/ | N/A |
| MultiQC v1.12 QC | https://multiqc.info | N/A |
| fastp v0.20.1 | https://github.com/OpenGene/fastp | N/A |
| STAR v2.7.08a | https://github.com/alexdobin/STAR | N/A |
| HTSeq v0.13.5 | https://htseq.readthedocs.io/en/master/ | N/A |
| DESeq2 v 1.30.1 | https://bioconductor.org/packages/release/bioc/html/DESeq2.html | N/A |
| DAVID version 6.8 | https://david.ncifcrf.gov | N/A |
| SynGO | https://www.syngoportal.org/ | N/A |
| scripts in MATLAB to track single vesicles containing fluoNGF | (Convertino et al., 2020)[56] | https://github.com/Stefano-Luin/TrackFluoNGFvesicles |
| ImageJ | (Schneider et al., 2012)[101] | https://imagej.nih.gov/ij/ |

(*Continued on next page*)

*Continued*

| REAGENT or RESOURCE | SOURCE | IDENTIFIER |
|---|---|---|
| Puncta analyzer, a Fiji plugin | (Ippolito & Eroglu, 2010)[102] | https://github.com/physion/puncta-analyzer |
| NeuronJ, a Fiji plugin | (Meijering et al., 2004)[103] | https://imagej.net/plugins/neuronj |
| Diana, a Fiji plugin | (Gilles et al., 2017)[104] | https://imagej.net/plugins/distance-analysis |
| GraphPad software, version 7.0 | GraphPad | https://www.graphpad.com/scientific-software/prism/ |
| Other | | |
| Nanoparticles | Chemicell | #4115 |
| Microfluidic devices | XONA | #RD150 |
| Halbach-like cylinder magnetic applicator | (Riggio et al., 2014)[23] | N/A |
| Neodimium disc magnet | https://www.supermagnete.it | S-12-02-N |
| Diamond knife | Diatome | https://www.diatomeknives.com/knives/diamond_knife.aspx |
| Mesh copper grids | Electron Microscopy Science | G300Cu |

## RESOURCE AVAILABILITY

### Lead contact

Vittoria Raffa (vittoria.raffa@unipi.it).

### Materials availability

This study did not generate new unique reagents.

### Data and code availability

- Original images, row data, processes data, metadata and codes are stored in Google Drive and are available at the public link: https://drive.google.com/drive/folders/1d5XMRwT-u9S4Lxt_iXud6oANvUO7Sid2?usp=share_link.
- The codes used have been previously published and are freely available (see key resources table).
- Any additional information required to reanalyze the data reported in this paper is available from the lead contact upon request.

## EXPERIMENTAL MODEL AND SUBJECT DETAILS

### Mice

Animal procedures were performed in strict compliance with protocols approved by the Italian Ministry of Public Health and the local Ethical Committee of the University of Pisa (protocol number 39E1C.N.5Q7) in conformity with the Directive 2010/63/EU. C57BL/6J mice were kept in a regulated environment (23 ± 1°C, 50 ± 5% humidity) with a 12 h light-dark cycle with food and water *ad libitum*.

### *C. elegans*

We used the following *C. elegans* strains: GN692 [*ljSi123*[*mec-7*p:GCaMP6s:SL2:tagRFP];*lite-1(ce314)*] worm strain, which expresses GCaMP6s and the calcium-independent tagRFP in touch receptor neurons[99] and GN693 [*ljSi123*[*mec-7*p:GCaMP6s:SL2:tagRFP];*lite-1(ce314); mec-4(u253)*]; MSB32 [*hpIs258*; *lite-1(ce314)* X] which expresses the green calcium sensitive fluorophore in motor-neurons;[100] GN510 [*mec-4(zdIs5)* I; *mec-12(e1607)* III] worm strain that expresses GFP and the mutation (*mec-12(e1607)*) for α-tubulin in touch receptor neurons; GN647 [*ptl-1(pg73)* III; *mec-7(ok2152)* X],[40] worm strain mutant for MEC7 β-tubulin in touch receptor neurons lacking 15 protofilament microtubules. We also used MSB1094[snn-1(syb2590); mec-4(zdIs5)I] and MSB1095 [snn-1(syb2590); mec-4(zdIs5) I; mec-12(e1607) III] to investigate synaptic vesicle trafficking in wt and mutant animals lacking 15pf microtubules. For kinesin tracking, we used STR399 [unc-119(ed3); hrtSi45[mec-4:unc-104pex:gfp:epdz LGI]].[105]

## METHOD DETAILS

### Cell culture

For hippocampal neurons, newborn animals (P1 stage) were sacrificed and both hippocampi were harvested in a solution of D-glucose 6.5 mg $ml^{-1}$ in DPBS (Gibco, Thermo Fisher Scientific, Waltham, Massachusetts, US, #14190-094). Cell isolation was

performed by chemical digestion and mechanical dissociation as previously described.[25] After this step, cells were seeded in high-glucose DMEM (Gibco, Thermo Fisher Scientific, Waltham, Massachusetts, US, #21063-029) with 10% fetal bovine serum (FBS, Gibco; Thermo Fisher Scientific, Waltham, Massachusetts, US, #10270-106), 100 IU·ml$^{-1}$ penicillin, 100 μg ml$^{-1}$ streptomycin (Gibco, Thermo Fisher Scientific, Waltham, Massachusetts, US, #15140-122) and 2 mM Glutamax (Gibco, Thermo Fisher Scientific, Waltham, Massachusetts, US, #35050-038) on surfaces pre-coated with 100 μg ml$^{-1}$ poly-L-lysine (PLL, Sigma-Aldrich, Burlington, Massachusetts, US, #P4707) and 10 μg ml$^{-1}$ laminin (Sigma-Aldrich, Burlington, Massachusetts, US, #L2020), unless stated otherwise. The medium was replaced 4 h later by cell culture medium consisting of Neurobasal-A medium (Gibco, Thermo Fisher Scientific, Waltham, Massachusetts, US, #12348-017) modified with B27 (Gibco, Thermo Fisher Scientific, Waltham, Massachusetts, US, #17504-044), 2 mM Glutamax (Gibco, Thermo Fisher Scientific, Waltham, Massachusetts, US, #35050-038), 50 IU·ml$^{-1}$ penicillin, 50 μg ml$^{-1}$ streptomycin and 2.5 μM AraC (Sigma-Aldrich, Burlington, Massachusetts, US, #C1768).

For DRGs neurons, mice pups (P3 stage) were used. After sacrifice, 20–30 DRGs were collected per animal. DRGs were then digested in a solution of DPBS supplemented with 0.03% collagenase from *Clostridium histolyticum* (Sigma-Aldrich, Burlington, Massachusetts, US, #C7657), 0.3% dispase II protease (Sigma-Aldrich, Burlington, Massachusetts, US, #D4693) and 0.18% glucose (Sigma-Aldrich, Burlington, Massachusetts, US, #G7021). The digesting DRGs were incubated with DPBS containing 0.01% deoxyribonuclease I from bovine pancreas (Sigma-Aldrich, Burlington, Massachusetts, US, #DN25) and 0.05% trypsin inhibitor from Glycine max (Sigma-Aldrich, Burlington, Massachusetts, US, #T9003). After the chemical digestion, DRGs were mechanically dissociated with a fire-polished glass Pasteur pipette. Cells were resuspended in cell growth medium modified with 100 ng ml$^{-1}$ NGF (Sigma-Aldrich, Burlington, Massachusetts, US, #N5415) and seeded on surfaces pre-coated with 100 μg ml$^{-1}$ poly-D-lysine (PDL, Sigma-Aldrich, Burlington, Massachusetts, US, #A-003-E) and 10 μg ml$^{-1}$ laminin, unless otherwise stated.

Half of the medium was replaced every 2–3 days. Cell cultures were maintained at 37°C in a saturated humidity atmosphere containing 95% air and 5% $CO_2$.

The isolation of primary *C. elegans* neurons was performed following a previously described method.[106] Briefly, after synchronization, worms were seeded onto peptone-enriched plates and incubated at room temperature (RT). Once populated with eggs, the plates were washed with Milli-Q $H_2O$ and the eggs collected. The obtained pellet of worms and eggs was lysed through resuspension in a freshly prepared bleaching solution and rocked gently by hand for up to 10 min. The progress of the lysis reaction was monitored until approximately 70% of the worms were lysed. The reaction was then stopped using an egg buffer [118 mM NaCl, 48 mM KCl, 2 mM $CaCl_2$, 2 mM $MgCl_2$, 25 mM HEPES (pH 7.3), and an osmolarity of 340 mOsm]. After three washes with fresh egg buffer, the eggs were separated using a final 30% concentration of sucrose by centrifuging at 1200 rpm for 20 min. After collection and three washes with egg buffer, the eggs were treated with 0.5 U·ml$^{-1}$ chitinase (Sigma-Aldrich, Burlington, Massachusetts, US, #C6137). To digest the eggshells, chitinase was rocked gently at RT for 40 min. Once approximately 80% of the eggs have been digested, the reaction was stopped with L15 medium (Sigma-Aldrich, Burlington, Massachusetts, US, #L4386 with the addition of 10% (v/v) heat-inactivated FBS, 50 U·ml$^{-1}$ penicillin, and 50 μg ml$^{-1}$ streptomycin). The resulting solution passed through a 25 gauge needle 10 to 15 times. The obtained single-cell suspension was filtered through a 5 μm Durapore filter (Millipore, Burlington, Massachusetts, US, #SVLP04700) and centrifuged for 3 min at 3200 rpm. Cells were cultured on peanut lectin (1:10, Medicago, Denmark, #05-0116-10) coated surfaces at a density of ∼300 cells mm$^{-2}$ and incubated at 25°C (unless stated otherwise). After 4 h, new medium was added. Fresh medium was changed every 24 h.

### Drug treatment

Neurons were seeded at DIV0 and cultured in cell culture medium until DIV1. At DIV1, the medium was supplemented with Nocodazole (Sigma-Aldrich, Burlington, Massachusetts, US, #SML1665; 1.8 ng mL$^{-1}$) or Cycloexamide (Sigma-Aldrich, Burlington, Massachusetts, US, #C7698; 30 ng mL$^{-1}$) or Brefaldin-A (Sigma-Aldrich, Burlington, Massachusetts, US, #B5936; 0.05 μg ml$^{-1}$) or GsMTx-4 (Sigma-Aldrich, Burlington, Massachusetts, US, #SML3140; 500 nM) until DIV3 (Nocodazole, Brefaldin-A, or GsMTx-4) or DIV6 (Cycloexamide).

### Nanoparticles

MNPs are magnetite nanoparticles (Fluid-MAG-ARA, Chemicell, Germany; #4115) characterized by a core of iron oxide (approximately 75 ± 10 nm in diameter) and an outer layer of glucoronic acid. The hydrodynamic diameter is 100 nm. The saturation magnetization of 59 A·m$^2$·kg$^{-1}$, as stated from the supplier. MNPs have been added to the cell growth medium at the concentration of 5 μg ml$^{-1}$.

### Microfluidic chambers

Cells were grown in microfluidic chambers assembled by mounting XONA microfluidic devices (XONA, Research Triangle Park, North Caroline, US, #RD150) on glass coverslips (22 mm in diameter). In order to promote axons to invade the axonal compartment, for hippocampal neurons, a differential coating was performed (standard coating in the somato-dendritic compartment and 500 μg ml$^{-1}$ PLL and 100 μg ml$^{-1}$ laminin for the axonal compartment) while, for DRG neurons, an NGF gradient was created (100 and 50 ng ml$^{-1}$ for the axonal and somato-dendritic compartment, respectively).

### Magnetic nano-pulling assay

At DIV0, hippocampal or DRG neurons were seeded in microfluidic chambers at a density of 200,000 cells, while *C. elegans* touch receptor neurons in 35 mm glass-bottom Petri dishes #1.5 (Willcow Glass, The Netherlands, #HBST-3512) at a density of approximately 500,000 cells. Cell growth medium was modified with 5 $\mu g\ ml^{-1}$ MNPs 4 h after seeding in hippocampal and touch receptor neurons, and the day after (DIV1) in DRGs neurons. The magnetic field (stretch group) or a null magnetic field (control group) was applied from DIV1 (if not stated differently). A Halbach-like cylinder magnetic applicator was used, which provided a constant magnetic field gradient of 46.5 $T\ m^{-1}$ in the radial centrifugal direction.[22,23] For axonal transport studies, a neodymium disc magnet (grade N45, diameter 12 mm, height 2 mm) was used and applied for 12 h before observations.

Hippocampal neurons were fixed in 2% PFA for 10 min at RT at DIV6 (if not stated differently). DRGs and touch receptor neurons were not fixed.

### RNA extraction and quantification

The experiment was performed in microfluidic chambers and the RNA was separately extracted from the somato-dendritic and axonal compartment as described in.[31] The nucleoSpin RNA PLUS XS Kit (Machery-Nagel, Düren, Germany, #740990.50) was used for RNA extraction. Axonal compartment was lysed without affecting the soma compartment (and vice-versa) by generating a liquid head that counteracts diffusion.[30,31,107] Samples were collected in lysis solution and incubated at 4°C. Lysed samples were then treated to digest the DNA, and the RNA was eluted in RNAse-free water. The Quant-iT RiboGreen RNA Kit (Thermo Fisher Scientific, Waltham, Massachusetts, US, #R11490) was used for the quantification of total RNA. QuantiTect Reverse Transcription Kit (Qiagen, Hilden, Germany, #205311) was used to produce the cDNA via reverse transcription. qPCR was performed using GoTaqpPCR (Promega, Madison, Wisconsin, US, #A6001). The expression of two markers, the nuclear histone H1 and a ubiquitous β-actin was evaluated to rule out the presence of somas in the axonal compartment (key resource table and Table S1).

### RNA sequencing

The experiment was performed for stretch group and control group on two cellular components (axonal and somato-dendritic compartment), and in six biological replicates. In total, 24 RNA extracts were analyzed. Quality check (QC) was performed by calculating the ribosomal content (RNA integrity number). RNAseq was performed by GENOME Scan (The Netherlands) with the platform Illumina NovaSeq6000 sequencer. The RNA library was prepared using the polyA selection library and sequencing mode PE (paired end), read length 150 bp, ~9 Gb and 30 million XP reads per sample. Default genomes and mouse annotation were Ensembl GRCm38.p6 (available on https://www.ncbi.nlm.nih.gov/assembly/GCF_000001635.26/). Raw data quality was analyzed using FastQC v0.11.9, MultiQC v1.12 QC tools (Figure S4). Sequence reads were trimmed to remove possible adapter sequences using fastp v0.20.1 with default settings. The reads were mapped against the reference sequence using STAR v2.7.08a with default settings (Figure S5) and the number of reads per gene was determined with HTSeq v0.13.5 and the Ensembl GRCm38.p6 GTF annotation file (Figure S6). Differential gene expression analysis was performed using DESeq2 v 1.30.1. Datasets are available in the public repository GEO (accession number: GSE197808).

### Quality check at the biological and bioinformatic level

In the microfluidic chamber model, only axons should be able to spread into the axonal compartment, due to the small cross-section of the microgrooves. However, to ensure the absence of any somatic cross-contamination, samples were inspected for the presence of nuclei in the axonal compartment, all of which were negative to Hoechst staining (n = 6) (Figure S1). To further rule out additional sources of contamination (*e.g.* spillage of lysis buffer between the two compartments), a qPCR analysis was performed on RNA extracts for the detection of a nuclear marker, the histone protein H1. β-actin mRNA (housekeeping) was detected in both compartments while H1 mRNA was present in the somato-dendritic compartment but not in the axonal one (n = 6), which meant that the cross-contamination was negligible (Table S1). As a further quality control, we decided to eliminate axon samples with trace levels of soma contamination at the bioinformatic level. Specifically, we performed a PCA based on all expressed genes. PC1 reflected the major variance (85% and 3% of variance associated with PC1 and PC2, respectively, Figure 1B). PC1 and the sample-to-sample distance map (not shown) confirmed that samples extracted from the axonal compartment cluster and segregate from samples extracted from the somato-dendritic one based on the gene expression patterns. One axon sample, out of 12, was intermediate (marked with a circle, Figure 1B). To confirm the presence of a cross-contamination for this sample, the number of detected genes was counted. Excluding this sample from the count of detected genes, axonal samples contained on average 6,382 ± 2025 detected genes (n = 11), and somato-dendritic samples contained 23,329 ± 753 detected genes in total (n = 12) (*t* test, two-tailed, $p < 0.0001$). The sample marked with a circle in Figure 1B contained 14,159 detected genes, which is clearly an intermediate value between somato-dendritic and axonal samples, suggesting a contamination by soma. This sample, probably contaminated by somatic RNA, was then discarded from the subsequent analysis.

### GO and GOEA

GO analysis was carried out using DAVID version 6.8 (https://david.ncifcrf.gov/) and the sub-databases GOTERM_CC_DIRECT and the feature "functional annotation chart".[32] GOEA was conducted using SynGO (https://www.syngoportal.org/) to perform enrichment analysis of synaptic genes in the function domain.[33]

### Ribopuromycylation

The study of ribosomes in active translation was performed through the ribopuromycylation (RPM method, modified from.[108] Briefly, hippocampal neurons were cultured in microfluidic chambers from DIV0 and stimulated from DIV1 to DIV6. At DIV6, neurons were treated with 200 μM emetine (Sigma-Aldrich, Burlington, Massachusetts, US, #E2375) and 100 μM puromycin (Sigma-Aldrich, Burlington, Massachusetts, US, #P7255) for 10 min at 37°C. Samples were then washed with ice-cold 0.0003% digitonin (Sigma-Aldrich, Burlington, Massachusetts, US; #D141) for 2 min. Lastly, samples were washed with ice-cold DPBS and fixed in 2% PFA, 7.5% sucrose (Sigma-Aldrich, Burlington, Massachusetts, US, #S0389) for 20 min at RT.

### Immunostaining and imaging

For all the experiments (except those related to Figures 2A4, 2C4, 2D4 and 5), after fixation, hippocampal neurons were permeabilized in 0.5% Triton X-100 for 10 min at RT. Samples were then blocked in 5% serum, 0.3% Triton X-100 in DPBS for 1 h at RT. Primary antibodies were diluted in 3% serum, 0.2% Triton X-100 in DPBS as follows: TUBB3 (Sigma-Aldrich, Burlington, Massachusetts, US; #T8578, 1:500) Synapsin I (Synaptic Systems, Goettingen, Germany, #106 103, 1:500), Homer 1b/c (Synaptic Systems, Goettingen, Germany, #106 023, 1:350), VGlut1 (Sigma-Aldrich, Burlington, Massachusetts, US; # AMAB91041, 1:500), acetylated tubulin (Sigma-Aldrich, Massachusetts, US; #T7451,1:400), tyrosinated tubulin (Abcam, # ab6160, 1:400). After overnight incubation at 4°C, samples were washed and then incubated with secondary antibodies (Thermo Fisher Scientific, Waltham, Massachusetts, US, #O6380, #A32731, #A11011, #A32728, #R6393, #A21449, 1:500; Abcam, Cambridge, UK, #ab150169, 1:500) and Hoechst 33,342 (Thermo Fisher Scientific, Waltham, Massachusetts, US, #H3570, 1:1000) for 1 h at RT. For experiments related to Figures 2A4, 2C4, 2D4 and 5, we followed a protocol modified from Cioni and colleagues.[67] Briefly, at DIV6, samples were fixed in 2% PFA, 7.5% sucrose in DPBS for 20 min at RT. Samples were then washed with DPBS and Triton X-100 in very low concentration (0.001% in DPBS). Samples were permeabilized with a solution of 0.1% Triton X-100 in DPBS for 5 min, and blocked with 5% goat serum in DPBS for 30 min. Samples were incubated with primary antibodies (TUBB3, Sigma-Aldrich, Burlington, Massachusetts, US, #T8578, 1:500; TUBB3, Abcam, Cambridge, UK, #ab41489, 1:1000; Mark4, Abcam, Cambridge, UK, # ab124267, 1:200; tau ser262, Abcam, Cambridge, UK, #ab131354, 1:200; S6, Cell Signaling, Danvers, Massachusetts, US, #2217, 1:200; Rab7, Abcam, Cambridge, UK, #ab137029, 1:200; anti-Puromycin, Sigma-Aldrich, Burlington, Massachusetts, US, #MABE343, 1:1000) at 4°C overnight. Then samples were incubated with secondary antibodies (see above) and Syto RNA select (Thermo Fisher Scientific, Waltham, Massachusetts, US, #S32703, 1:2500), or Hoechst 33342 (see above) for 45 min at RT. Samples were imaged with a laser scanning confocal microscope (Nikon A1, Eclipse Ti). Images were acquired with a 60× objective oil immersion. Series of ~30 optical plans in Z were acquired at 1024 × 1024 pixel resolution with a z-step of 0.2 μm. Images were acquired using a 405 nm laser (425–475 emission filter) or a 488 nm laser (500–550 emission filter) or a 561 laser (570–620 emission filter) or a 640 nm laser (663–738 emission filter).

Before imaging the *C. elegans* neurons, the medium was changed. Image acquisition was performed using an inverted microscope (DMi8, Leica), either with a 40×/1.1 water immersion lens or a 25×/0.95 water immersion lens. A multi-wavelength LED light source (SpectraX, Lumencor) was used for fluorescence excitation. Touch receptor neurons expressing calcium-sensitive GCaMP6s and tag-RFP were excited with 470/24 nm and 550/15 nm band-pass filtered LEDs at 8–15% and 20–30% of the output power, respectively (measured 4–7 mW and 14–21 mW at the sample plane with a microscope slide power meter, Thorlabs S170C). Excitation power was kept constant for both the control and stretched conditions of the same replicate. Fluorescence emission was directed to an sCMOS camera (Hamamatsu Orca Flash 4 V3) with a quad-edge dichroic splitter (Semrock, FF409/493/573/652-Di02-25x36). Green and red fluorophore signals were later separated with an image splitting unit (Hamamatsu, W-view Gemini A12801-01), in which a 538 nm edge dichroic splitter (Semrock, FF528-FDi1-25-36), and 512/25 nm (Semrock, FF01-512/25-25) and 670/30 nm (FF01-670/30-25) band-pass emission filters were built. The sCMOS camera was used in W-view mode, enabling simultaneous dual fluorophore imaging at an exposure time of 200 ms for both top (GCaMP) and bottom (tag-RFP) camera halves. Motor neurons expressing solely GCaMP6s were directly imaged with no image splitting unit.

### Sample preparation for TEM

For the ultrastructural characterization, hippocampal neurons were treated as previously described.[56] Briefly, neurons were fixed with an aldehydic solution (1.5% glutaraldehyde in 0.1 M Cacodylate buffer - pH 7.4), washed, and post-fixed with reduced osmium tetroxide solution (1% $K_3Fe(CN)_6$ + 1% $OsO_4$ in 0.1 M Cacodylate buffer). After rinses, neurons were stained with our homemade staining solution (X solution diluted 1:10 (v/v) in 20% ethanol/water,[109] then dehydrated, with an increasing series of ethanol concentrations. Samples were then embedded in epoxy resin (Epoxy embedding medium kit, Merck KGaA, Darmstadt, Germany) which was then baked for 48 h at 60°C. After the coverslips have been removed, embedded neurons were mounted on a resin support and sectioned with a UC7 ultramicrotome (Leica Microsystems, Vienna, Austria) with a 35° diamond knife (Diatome Ltd, Switzerlands). Sections of 80 nm were collected on 300 mesh copper grids (G300Cu - Electron Microscopy Science, Hatfield, PA, USA).

Grids were analyzed with a Zeiss Libra 120 Plus transmission electron microscope, operating at 120 kV, and equipped with an in-column omega filter (for the energy filtered imaging).

### NGF single vesicle tracking

fluoNGF was obtained by performing an enzymatic fluorolabeling reaction on the YBBR-tagged NGF recombinantly produced in E. coli.[97] A total of 90–100 mg purified YBBR-NGF (kindly donated by Prof. A. Cattaneo, Bio@SNS Lab, Pisa) was incubated with 73 μM

CoA-Alexa647, 17μM Sfp Synthase, 36 mM $MgCl_2$ in DPBS up to 270 μL final volume for 30 min at 37°C; the excess of free fluorophore was removed by desalt spin-column and the fluoNGF obtained was stored at 4°C for a maximum of 10 days. This reaction enabled the NGF C-terminus to be stoichiometrically labeled with Alexa 647 fluorophore using a method first described in Yin and colleagues[110] (Yin et al., 2005) and optimized as in,[111] to finally achieve the covalent binding of two fluorophores per neurotrophin dimer. At DIV3 (after overnight stimulation), DRG cultures were prepared for time-lapse studies. To track the vesicles, 2 nM fluoNGF was applied in the axon side, incubated for 1 h at 37°C, after which the axonal medium was replaced.

In order to acquire time-lapse videos, we used an inverted epi-fluorescence microscope (Leica AF6000) equipped with Leica TIRF-AM module, incubator chamber at 37°C, 5% $CO_2$, an electron multiplying charge-coupled device camera (ImagEM C9100-13, Hamamatsu), and a 100× oil immersion objective (NA 1.47), which enabled the acquisition of fields of 512 × 512pixels (116.80 × 116.80 μm) typically comprising two microchannels. fluoNGF vesicles were imaged inside the microchannels in epifluorescence configuration, using a 635 nm laser line at maximum power, a Cy5 Leica1152303 fluorescence cube and an exposure time of 100 ms. Up to 1000 frames for each time-lapse video were acquired, and each chip was imaged for about 45 min.

## QUANTIFICATION AND STATISTICAL ANALYSIS

### Image analysis

NeuronJ, a Fiji plugin, was used to evaluate axon length.[101,103] Briefly, axons (TUBB3 stained) were traced with the tracing tool by choosing the exit point from the microchannels as the starting point. For *C. elegans* neurons, the green GCaMP channel was used to determine the length of the axon. To test stretch-growth following Cycloheximide treatment, network analysis was performed. Briefly, the area of the neurites (“threshold” function) in the network was obtained from 10× magnification images (randomly acquired). The network area was calculated by normalizing the area of the neurites and the number of the nuclei, manually counted with the function “Cell Counter” of Fiji software.

For NGF vesicle tracking analysis, scripts in MATLAB (The MathWorks) were used in order to detect single vesicles containing fluoNGF along the axon and to track them, so as to assign them a dynamic mode based on the direction of movement and velocity, as described in.[56] Kymograph analysis was carried out using ImageJ image analysis software.

For fluorescence quantification, we evaluated the total fluorescence ($f$) and/or the mean fluorescence ($\bar{f}$), defined as:

$$f = IntDen - (\bar{f}_{back} \bullet A)$$

$$\bar{f} = \frac{f}{A}$$

where *IntDen* is the integrated density (defined as the sum of all the pixel intensities in that selected region), A is the area of the ROI (region of interest) and $\bar{f}_{back}$ is the mean fluorescence of background readings. To study the fluorescence distribution, the mean fluorescence was evaluated all along the axons. For the tip, the last 5 μm were considered, while for the neurite shaft the first and last 5 μm were excluded.

The ratio of acetylated versus tyrosinated α-tubulin was determined from total fluorescence ($f$) intensities calculated in the whole axon. Co-localization studies between LEs and RNA granules or active ribosomes were performed with Diana, a Fiji plugin.[104] Taking advantage of the integrated features of the plugin, each channel was first segmented (default parameters for LE and active ribosomes; min. objects size = 1 pixel for LE and RNA granules), then the percentage of co-localization between the two objects of interest (LE and RNA granules or LE and active ribosomes) was evaluated.

The Diana plugin was also exploited for the evaluation of RNA granules density. Briefly, images were segmented in Diana (min. objects size = 1 pixel) and the total volume of the RNA granules contained in one neurite was collected and then normalized for the corresponding area. The same plugin was also used to study the number, volume and fluorescence (as integrated density) of synapsin I spots contained in a defined neurite compartment. After the selection of the region of interest, the synapsin I channel was segmented with default parameters. The values related to the mentioned parameters were then collected and normalized for the analyzed area.

To estimate the co-localization between the spots of the pre-synaptic marker VGlut1 and the post-synaptic marker homer 1b/c, the plugin puncta analyzer was applied, as previously described.[102] Briefly, both channels were converted using the maximum intensity of the Z projection and merged. Following the identification of a specific ROI corresponding to all the neurites of the cell, and keeping default parameters, the plugin quantifies the puncta in each channel and the co-localized puncta between the two channels. The value obtained was then normalized for the considered area.

### TEM analysis

TEM analysis was carried out using ImageJ and the plugin NeuronJ.[103] For MT density, the MTs, recognized as tubular structures, were counted manually in a selected and organelle-free region of the neurite (Figure S7, dashed yellow lines). The diameter of the corresponding region was then measured, and the number of MTs normalized, obtaining one value per neurite. To study the ER

the cisternae were traced with NeuronJ and then normalized for the considered neurite area (Figure S7, magenta lines). NeuronJ was also exploited for the analysis of the post-synaptic density (PSD) region. Specifically, it was used to measure the length of PSDs (Figure S7, white line) in DIV14 control and stretched samples, and the mean value was considered for each synapse. The number of PSDs of each synapse was also counted manually in the two conditions. To determine the mitochondria density, mitochondria were counted manually (Figure S7, white "*") in DIV14 stretched and unstretched samples. The corresponding number was then normalized for the total area of the neurite, obtaining one value per neurite.

### Statistical analysis

Data were plotted with GraphPad 7.0. Values are reported as the mean ± standard error of the mean (SEM). The normality of the distribution was tested using the D'Agostino & Pearson normality test, Shapiro-Wilk normality test, or Kolmogorov-Smirnov normality test. For normally distributed data, we used the *t* test for unpaired data followed by Bonferroni correction or two-way ANOVA test. For non-normally distributed data, the Mann-Whitney test or Kruskal-Wallis test with post hoc Dunn's test, were carried out. Significance was set at $p \leq 0.05$.

**Cell Reports, Volume *42***

## Supplemental information

# Axonal plasticity in response to active forces generated through magnetic nano-pulling

**Alessandro Falconieri, Sara De Vincentiis, Valentina Cappello, Domenica Convertino, Ravi Das, Samuele Ghignoli, Sofia Figoli, Stefano Luin, Frederic Català-Castro, Laura Marchetti, Ugo Borello, Michael Krieg, and Vittoria Raffa**

**Supplemental information**

**Axonal plasticity in response to active forces generated through magnetic nano-pulling**

Alessandro Falconieri, Sara De Vincentiis, Valentina Cappello, Domenica Convertino, Ravi Das, Samuele Ghignoli, Sofia Figoli, Stefano Luin, Frederic Català-Castro, Laura Marchetti, Ugo Borello, Michael Krieg, Vittoria Raffa

**Table S1. qPCR analysis (related to Figure 1)**

| Group | Replicate | Cycle, β-actin mRNA | Cycle, H1 mRNA |
|---|---|---|---|
| Control, A | 1 | 34.38 | - |
| | 2 | 38.22 | - |
| | 3 | 36.77 | - |
| Stretch, A | 1 | 34.87 | - |
| | 2 | 38.87 | - |
| | 3 | 38.16 | - |
| Control, S | 1 | 19.97 | 24.92 |
| | 2 | 19.61 | 24.40 |
| | 3 | 19.80 | 25.33 |
| Stretch, S | 1 | 19.18 | 24.54 |
| | 2 | 17.63 | 23.46 |
| | 3 | 19.68 | 25.230 |

**Table S2. GO of cellular Component (CC) (related to Figure 1)**

| **GOTERM_cc_direct** | **Term** | **Gene count** | ***P* value** |
|---|---|---|---|
| GO:0005737 | cytoplasm | 313 | 3.00E-05 |
| GO:0005765 | lysosomal membrane | 24 | 4.90E-05 |
| GO:0005794 | Golgi apparatus | 74 | 8.80E-05 |
| GO:0005768 | endosome | 39 | 4.20E-04 |
| GO:0031902 | late endosome membrane | 12 | 6.30E-04 |
| GO:0005764 | lysosome | 26 | 1.40E-03 |
| GO:0016020 | membrane | 314 | 1.60E-03 |
| GO:0005739 | mitochondrion | 91 | 2.70E-03 |
| GO:0005856 | cytoskeleton | 61 | 7.40E-03 |
| GO:0005815 | microtubule organizing center | 14 | 7.90E-03 |

| | | | |
|---|---|---|---|
| GO:0031225 | anchored component of membrane | 13 | 9.40E-03 |
| GO:0005622 | intracellular | 81 | 1.30E-02 |
| GO:0005783 | endoplasmic reticulum | 67 | 2.40E-02 |
| GO:0005770 | late endosome | 11 | 3.30E-02 |
| GO:0045202 | synapse | 28 | 6.40E-02 |
| GO:0005829 | cytosol | 83 | 7.40E-02 |

**Table S3. Annotated genes dysregulated in GO:0005856 (cytoskeleton) (related to Figure 1)**

| Symbol | Name | Up/Down | Assigned cathegory |
|---|---|---|---|
| Flnb | filamin, beta | up | Actin-binding |
| Mical1 | microtubule associated monooxygenase, calponin and LIM domain containing 1 | up | Actin cytoskeleton |
| Pdlim1 | PDZ and LIM domain 1 (elfin) | up | Actin-binding |
| Svil | supervillin | up | Actin-binding |
| Tln2 | talin 2 | up | Actin-binding |
| Tmod1 | tropomodulin 1 | up | Actin cytoskeleton |
| Tpm2 | tropomyosin 2, beta | up | Actin cytoskeleton |
| Tagln | transgelin | up | Actin cytoskeleton |
| Ahnak | AHNAK nucleoprotein (desmoyokin) | up | Actin cytoskeleton |
| Axl | AXL receptor tyrosine kinase | up | Actin-binding |
| Dgkh | diacylglycerol kinase, eta | up | Actin-binding |
| Trip6 | thyroid hormone receptor interactor 6 | up | Actin-binding |
| Cdc42ep1 | CDC42 effector protein (Rho GTPase binding) 1 | up | Actin cytoskeleton |
| Rgcc | regulator of cell cycle | up | MT cytosckeleton |
| Sh3pxd2b | SH3 and PX domains 2B | up | Actin cytoskeleton |
| Dynlrb2 | dynein light chain roadblock-type 2 | up | Motor protein / transport |
| Rab29 | RAB29, member RAS oncogene family | up | Motor protein / transport |
| Zmynd10 | zinc finger, MYND domain containing 10 | up | Motor protein / transport |
| Kif18b | kinesin family member 18B | up | Motor protein / transport |

| | | | |
|---|---|---|---|
| 1110017D15 Rik | RIKEN cDNA 1110017D15 gene | up | MT-binding |
| Trim36 | tripartite motif-containing 36 | up | MT-binding |
| Rad51d | RAD51 paralog D | up | MT-binding |
| Ttll9 | tubulin tyrosine ligase-like family, member 9 | up | MT-binding |
| Ccsap | centriole, cilia and spindle associated protein | up | MT-binding |
| Cenpe | centromere protein E | up | MT-binding |
| Fam83d | family with sequence similarity 83, member D | up | MT-binding |
| Mtus1 | mitochondrial tumor suppressor 1 | up | MT-binding |
| Reep4 | receptor accessory protein 4 | up | MT-binding |
| Gramd3 | GRAM domain containing 3 | up | MT cytosckeleton |
| Frmd5 | FERM domain containing 5 | up | MT cytosckeleton |
| Anapc7 | anaphase promoting complex subunit 7 | up | MT-binding |
| Arl6 | ADP-ribosylation factor-like 6 | up | MT-binding |
| Aurkb | aurora kinase B | up | MT cytosckeleton |
| Cenpv | centromere protein V | up | MT-binding |
| Esrra | estrogen related receptor, alpha | up | MT-binding |
| Hmmr | hyaluronan mediated motility receptor (RHAMM) | up | MT-binding |
| Prkci | protein kinase C, iota | up | MT cytosckeleton |
| Abca2 | ATP-binding cassette, sub-family A (ABC1), member 2 | up | MT-binding |
| Pcnt | pericentrin (kendrin) | up | MT-binding |
| Tubgcp5 | tubulin, gamma complex associated protein 5 | up | MT cytosckeleton |
| Bcas3 | BCAS3 microtubule associated cell migration factor | up | MT cytosckeleton |
| Klhl21 | kelch-like 21 | up | MT cytosckeleton |
| Tada2a | transcriptional adaptor 2A | up | MT cytosckeleton |
| Hap1 | huntingtin-associated protein 1 | up | Motor protein / transport |
| Arc | activity regulated cytoskeletal-associated protein | down | Actin cytoskeleton |
| Ccdc66 | coiled-coil domain containing 66 | down | MT-binding |

| | | | |
|---|---|---|---|
| Dapk1 | death associated protein kinase 1 | down | Actin cytoskeleton |
| Fntb | farnesyltransferase, CAAX box, beta | down | MT cytosckeleton |
| Gdpd2 | glycerophosphodiester phosphodiesterase domain containing 2 | down | Actin cytoskeleton |
| Katnal1 | katanin p60 subunit A-like 1 | down | MT cytosckeleton |
| Klhl3 | kelch-like 3 | down | Actin-binding |
| Mark4 | MAP/microtubule affinity regulating kinase 4 | down | MT cytosckeleton |
| Mical3 | microtubule associated monooxygenase, calponin and LIM domain containing 3 | down | Actin cytoskeleton |
| Rhobtb3 | Rho-related BTB domain containing 3 | down | Actin cytoskeleton |
| Shtn1 | shootin 1 | down | MT cytosckeleton |
| Spire2 | spire type actin nucleation factor 2 | down | Actin cytoskeleton |
| Topbp1 | topoisomerase (DNA) II binding protein 1 | down | Actin cytoskeleton |
| Tppp | tubulin polymerization promoting protein | down | MT cytosckeleton |
| Tsc1 | TSC complex subunit 1 | down | Actin cytoskeleton |
| Ttll4 | tubulin tyrosine ligase-like family, member 4 | down | MT-binding |

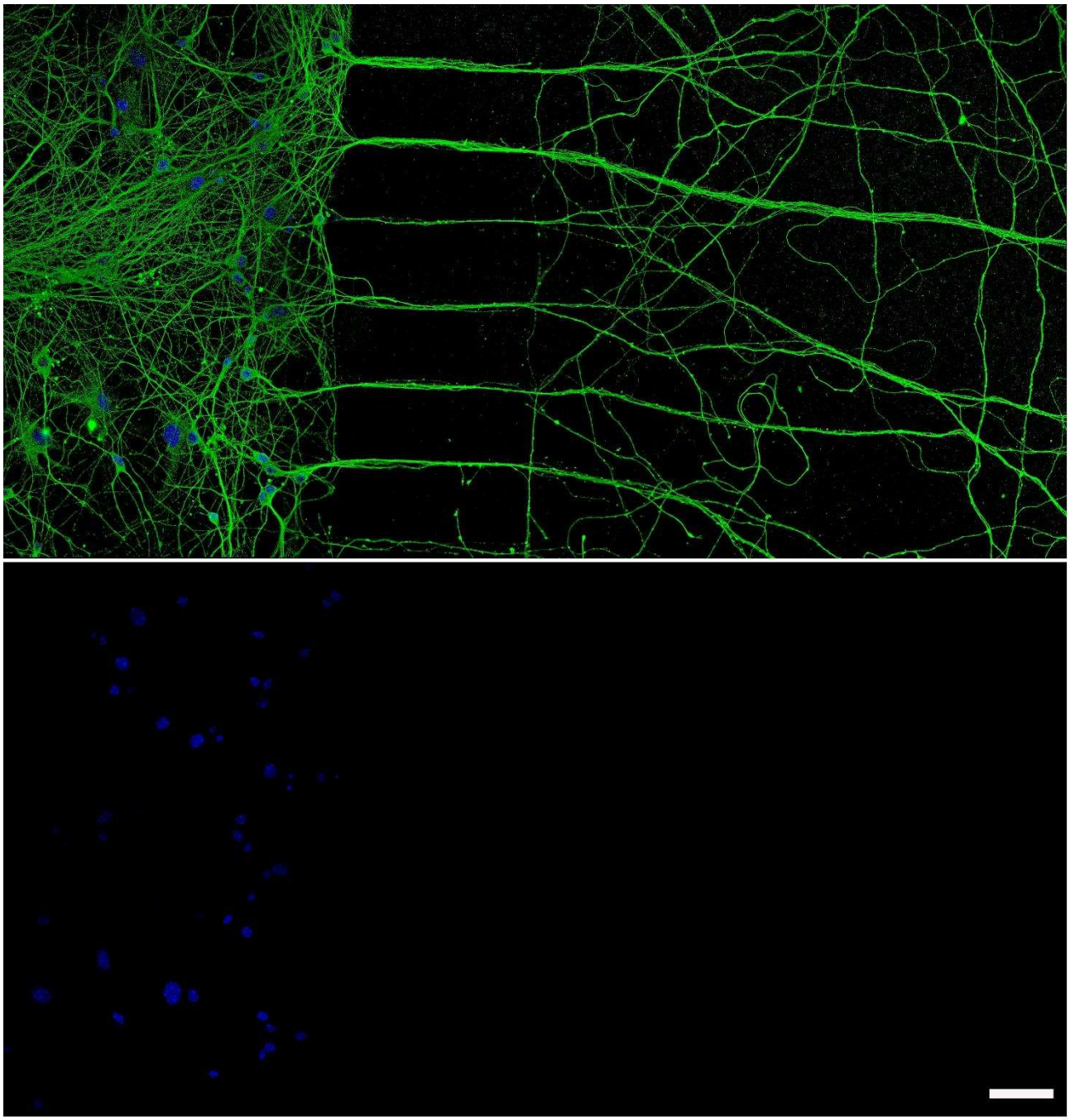

**Figure S1 (related to Figure 1).** Representative image of the somato-dendritic and the axonal compartment. In bottom panel is shown the absence of somata in the axonal compartment as no nuclei were found; BTUBBIII (green), Hoechst (blue) staining; scale bar: 50 μm.

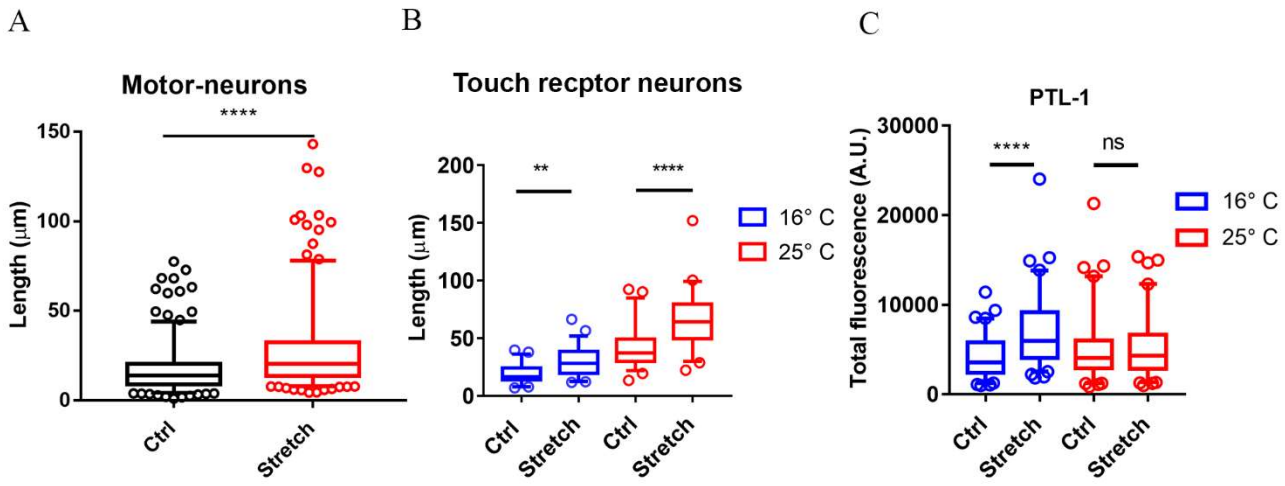


**Figure S2 (related to Figure 2).** (A) Neurite length of motor-neurons in control and stretched conditions (MSB32 strain). Box plot, 5-95 percentile, n=250 from five independent assays. Mann-Whitney test, $p<0.0001$. (B) Axonal length of WT touch receptor neurons for α and β-tubulin (GN692 strain). Control and stretched axons have been measured both, at 16°C and at 25°C. Box plot, 5-95 percentile, n=50 neurites. Kruskal-Wallis test with post hoc Dunn's test, $p<0.0001$. (C) Quantification of mNG total fluorescence in a transgenic model of tagged mNG::PTL-1 at 16°C and at 25°C. Box plot (5-95 percentile), n=80 neurites from four biological replicates. Kruskal-Wallis test with post hoc Dunn's test, $p<0.0001$.

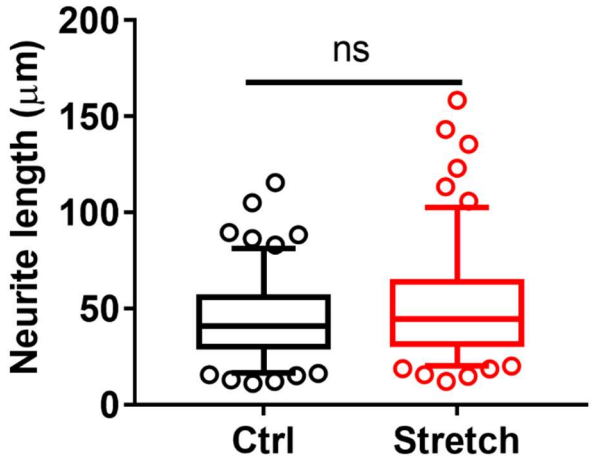


**Figure S3 (related to Figure 4).** Neurite length of touch receptor neurons of a *C. elegans* strain encoding for a fluorescent UNC-104 with Nocodazole treatment (1.8 $ng \cdot ml^{-1}$). Box plot (5-to-95 percentile), n=120 neurites from four biological replicates. Mann Whitney test, $p=0.08$.


**Figure S4 (related to Figure 1).** Quality control checks on raw sequence datasets.

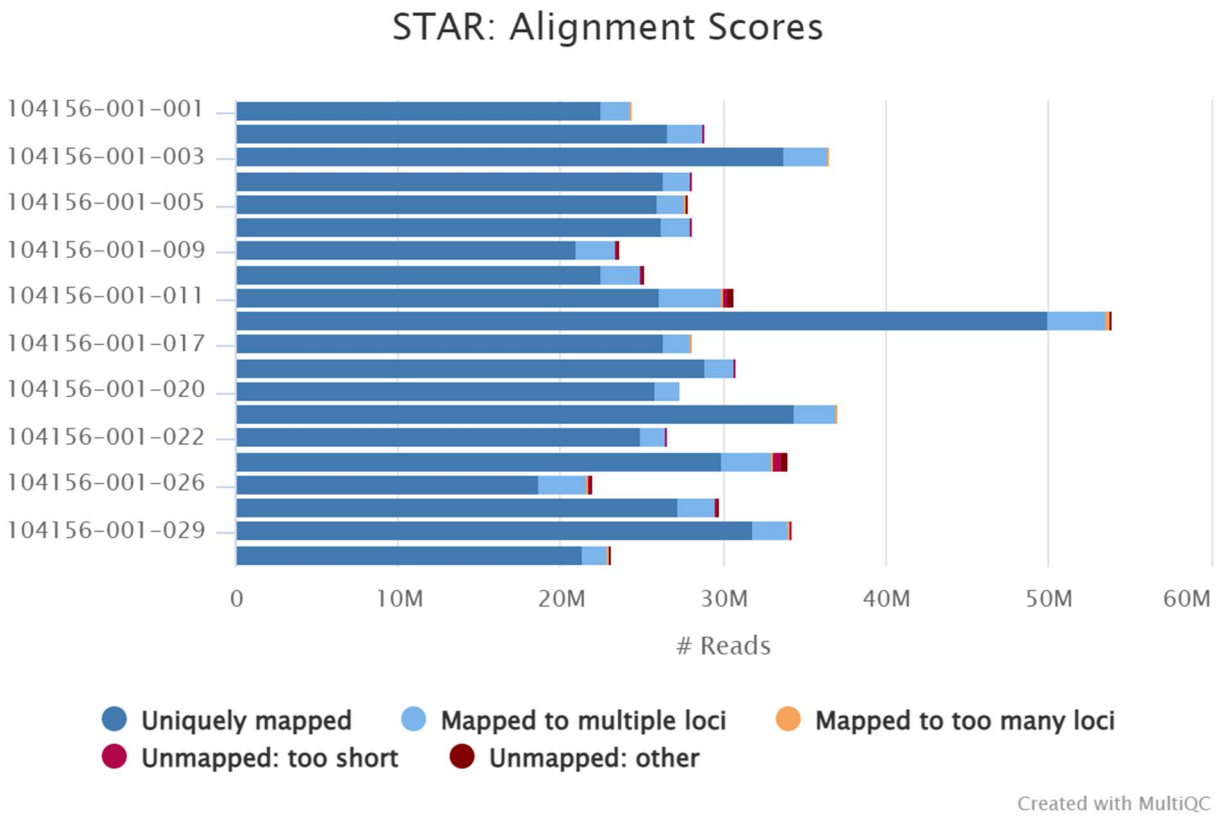


**Figure S5 (related to Figure 1).** Scores of the reads alignment to the reference genome.

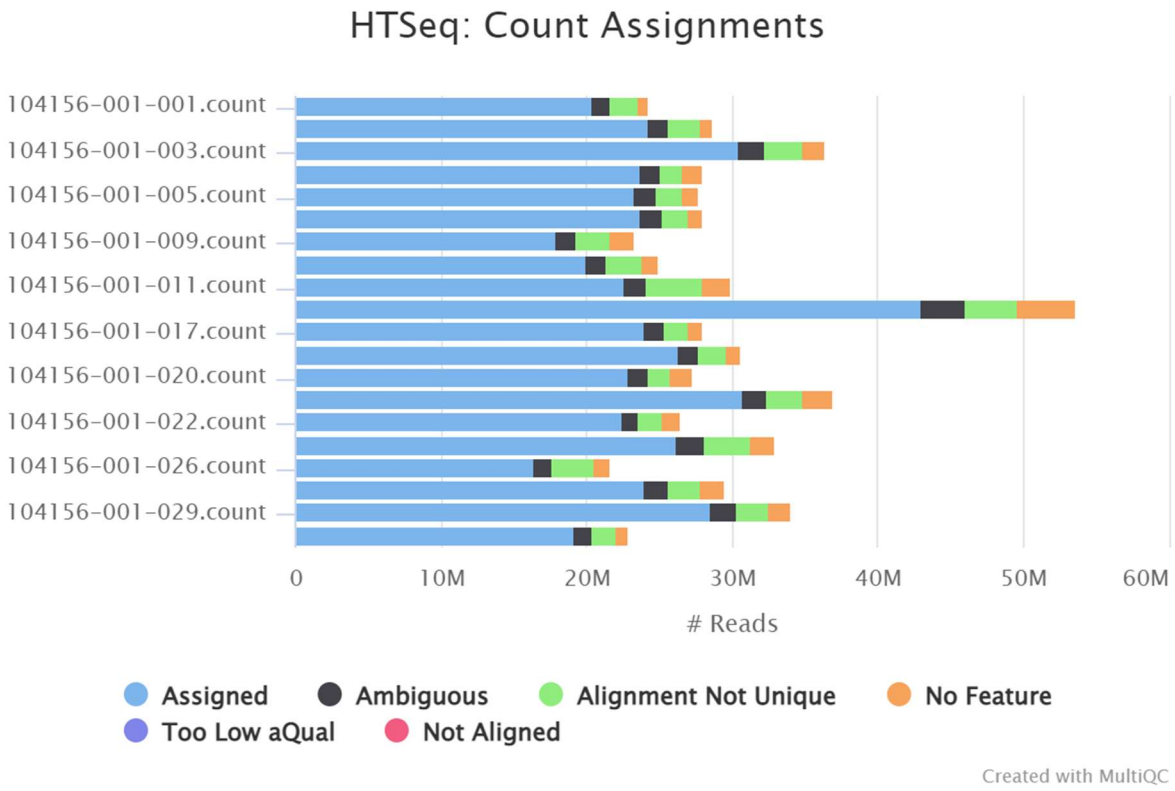


**Figure S6 (related to Figure 1).** Count of the reads mapped against the genes of the reference genome.

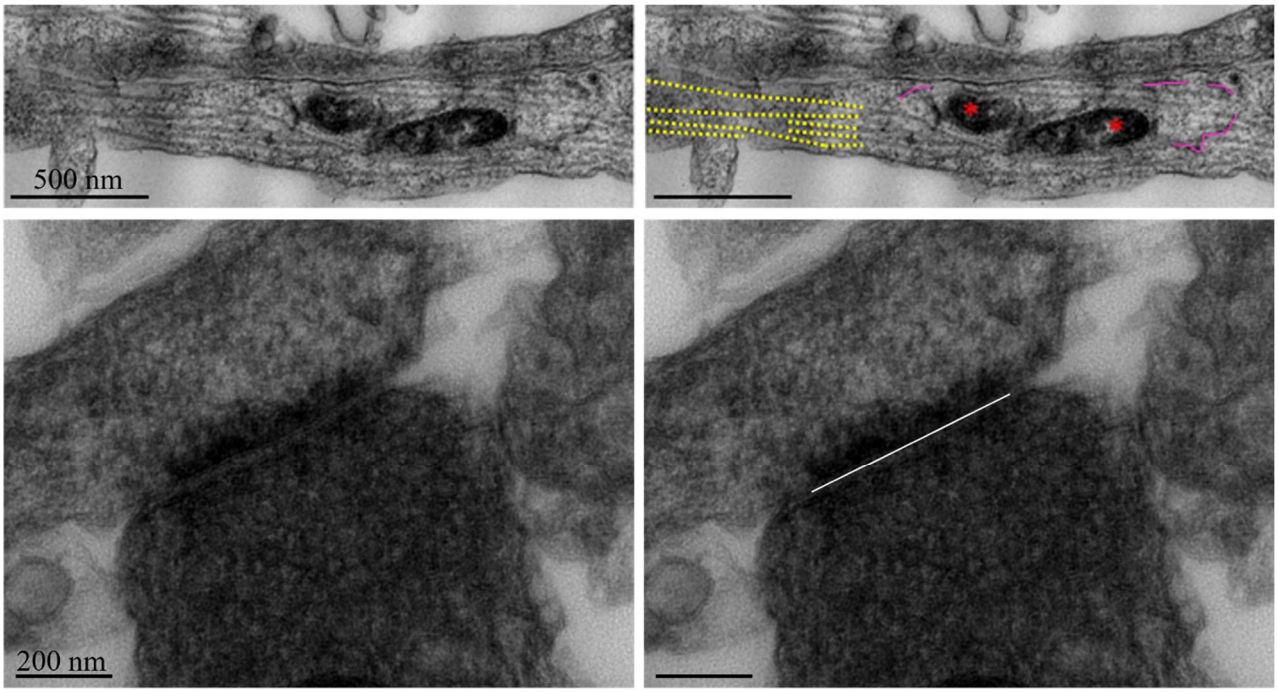


**Figure S7 (related to Figure 2 and 7).** Representative TEM images. MTs: dashed yellow lines; ER: magenta lines; mitochondrion indicated with "*"; PSD region: white line.